NONLINEAR
OPTICS

Characterization of the Optical Nonlinearities of Silver and Gold Nanoparticles

R. A. Ganeev*

The Guo China−US Photonics Laboratory, Changchun Institute of Optics, Fine Mechanics and Physics, Chinese Academy of Sciences, Changchun, 130033 China
*e-mail: rashid_ganeev@mail.ru

Abstract—The synthesis of nanostructured materials took much attention due to their advanced optical and nonlinear optical properties, which can be used in various areas of communications, optics, laser physics and medicine. During last two decades, special attention was given to the nonlinear optical properties of the nanoparticles (NPs) of variable morphology. Here we review the recent studies of the nonlinear optical properties of silver and gold NPs. We discuss the Z-scans and pump−probe transient absorption studies allowing determining the nonlinear refractive indices, nonlinear absorption coefficients and electron−phonon interaction times. The analysis of the low- and high-order harmonic generation in the laser-produced plasmas containing Ag NPs and Au NPs is also presented.

1. INTRODUCTION

Metal nanoparticles (NPs) have unique properties allowing applications in mechanics, catalysis, magnetism, optics, electricity, new material development, and heat physics, due to their morphology and size effects [1]. Among them, noble metal NPs have potential applications in the field of nanophotonics due to their strong nonlinear optical response, thus attracting a significant attention. As a typical representative of noble metals, silver and gold nanoparticles are particularly prominent.

Silver nanoparticles (Ag NPs) have attracted large attention during last time due to possibility in converting ultrafine silver nanoclusters to monodisperse silver sulfide nanoparticles [2], advanced performance of silver nanoparticles in the catalysis of the oxygen reduction reaction in neutral media [3], newly developed methods of diagnosis of breast cancer by surface-enhanced Raman spectroscopy of silver nanoparticles [4], enhanced antibacterial activity of bifunctional Fe_3O_4−Ag core−shell nanostructures [5], etc. Alongside the morphological properties, the optical and nonlinear optical features of these small-dimensional structures became the subject of numerous studies.

The analysis of the nonlinear absorption coefficients and nonlinear refractive indices of Ag NPs, as well as the exploration of their potential applications, were reported in a few studies [6−8]. There are experimental studies showing that particle size, morphology and surrounding medium of noble metal NPs have great influence on their nonlinear optical properties [9−11]. For example, Ag NPs with smaller particle sizes demonstrated weak nonlinear optical response, while larger particles were characterized by strong saturable absorption (SA) [9]. With the increase of particle sizes, nonlinear absorption has shown a shift from two-photon absorption (2PA) to SA, while nonlinear refraction was transformed from self-defocusing to self-focusing [10]. The SA caused by the ground state bleaching can lead to decrease of absorption in the sample. At the same time, the change of incident intensity of probe laser pulse can also cause the variation of nonlinear optical properties, such as the shift from SA to reverse saturable absorption (RSA). As the incident intensity increases, the RSA leads to enhancement of nonlinear absorption in the sample.

The attractive application of these nanostructured materials in optics is the protection of sensitive area of detection system through optical limiting (OL) of high-power laser radiation. One can anticipate that variations of the sizes of NPs can significantly enhance OL. In [12], the metal nanoparticle-embedded polymer film and their optical limiting capability were demonstrated. OL behavior of silver nanoparticles with different sizes and shapes is investigated and compared to the optical limiting performance of conventional carbon black suspension [13]. It found that the optical limiting effect is strongly particle size dependent and the best performance is achieved with the smaller particles.

Ag NPs are extraordinarily efficient at absorbing and scattering light and, unlike many dyes and pigments, have a color that depends upon the size and the shape of the particle. The strong interaction of the Ag NPs with light occurs because the conduction electrons on the metal surface undergo a collective oscillation when excited by light at specific wavelengths. The advantages of Ag NPs include monodisperse distribution in surrounding environment without agglomeration and aggregation, comprehensive characterization including TEM and UV-Vis spectroscopy, good stability, and long life time. A unique property of spherical Ag NPs is that its surface plasmon resonance (SPR) can be tuned from 400 to 530 nm by changing the particle size and the local refractive index near the particle surface. Even larger shifts of resonance peak towards the IR region can be achieved by producing silver nanoparticles with rod or plate shapes.

Different physical and chemical techniques are used for preparation of metallic NPs with variable morphology and sizes. Among them, laser ablation of bulk material has been proven to be a simple method for the synthesis of spherical nanoparticles in various liquids [14]. In many cases the distilled water is used during laser ablation of silver. Laser ablation of silver was also performed in NaCl aqueous solution [15]. It was shown that efficiency of Ag NPs formation depends on the concentration of NaCl in aqueous solution. Increase of NaCl concentration up to some threshold values led to decrease of the probability of NPs aggregation. Preparation of NPs in various solutions has many applications. For example, Ag NPs prepared during ablation in water are useful for surface-enhanced Raman scattering spectroscopy.

Another nonlinear process, which actively pursued using different NPs, is the frequency conversion of strong laser field in the plasmas containing such species. The low-order nonlinearities of NPs, which are responsible for third harmonic generation in laser-produced plasmas (LPP), were studied in [16]. The LPPs are also considered as the attractive nonlinear media for conversion of the frequency of ultrashort infrared laser pulses towards the extreme ultraviolet range. The advantages of using in situ produced Ag NPs for high-order harmonic generation (HHG) due to large nonlinear optical response of Ag NPs in the field of femtosecond probe pulses were analyzed in [17]. The spectral characteristics of harmonics from nanoparticles produced in situ were compared with the HHG from monoparticle plasma and with the HHG from preformed nanoparticle-containing plasma.

Gold nanoparticles (Au NPs) have been extensively studied due to possibilities for their use in different areas of nonlinear optics, optoelectronics, and laser physics. The applications of Au NPs include optical limiting, optical switching, plasmonic waveguides, photovoltaics, catalysis, drug delivery in medical science, nanotechnologies, spectroscopy and spectrophotometry, electrochemical and bioelectrochemical analysis, etc. Their unique optoelectronic properties are related with the surface plasmons at around $\lambda = 530$ nm, which being excited in the vicinity of this wavelength cause the enhancement of optical and nonlinear optical response [18]. Meanwhile, for the infrared and blue excitation wavelengths (800 and 400 nm corresponding to the Ti:sapphire laser radiation and its second harmonic, respectively), which emit out from the SPR of Au NPs, other factors like intraband transitions should also be taken into account. The SPR and thereby the optical response of Au NPs can be tuned by varying the size or shape of the nanoparticles leading to necessity in their analysis to define the customized optical properties for different applications.

Au NPs in the form of colloidal solutions were previously prepared using either chemical or laser ablation methods. The difference between these methods consists in different size characteristics of the nanoparticles produced. In previous studies, a dynamics of the spatial and nonlinear optical parameters of Au NPs was noted, but the mechanisms responsible for these variations have not been clarified to a sufficient extent. Optical nonlinearities of Au NPs were the subject of a number of studies during the past two decades. Those studies of gold aggregates at the wavelength of 532 nm, i.e., at resonance conditions with the SPR band of Au NPs, have shown that the changes of the refraction index can be due to different physical mechanisms.

Saturable absorption and reverse saturable absorption using the 532 nm excitation are two familiar nonlinear absorption types in gold nanoparticles [19]. SA and RSA are related to the decreasing and increasing in the absorption, respectively. For Au NPs, the SA effect at resonance conditions (i.e., close to $\lambda = 530$ nm) can mainly be attributed to the ground-state plasmon bleaching of the intraband transition in the s-p conduction band at moderate pump intensities. As the SA bands belong to the visible range, the Au NPs possess the potential of Q-switchers for short pulses generation in this region [20]. Additionally, the RSA effect can be related with the free-carrier absorption or 2PA. The changes from a negative value of nonlinear absorption to a positive one with increasing pulse energy suggest that the primary nonlinear absorption in Au NPs has been transformed from SA to RSA process, which can be useful for optical limiting of propagating radiation.

Optical limiting is one of potential applications of the materials' optical nonlinearities. Previously, small-sized species, like nanoparticles and quantum dots, have shown the advantages in their use for OL [21, 22]. The mechanisms that cause OL have different origins. RSA, which takes place due to enhanced absorption from excited states, is responsible for OL in

colloidal metal compounds and fullerenes. 2PA is responsible for OL in semiconductor structures. Excited state induced process is one of the main sources of optical nonlinearities, which has potential applications for OL. Thus a search of enhanced population of these states in the case of various nanoparticle solutions is worth to continue by using the size-related variations of their nonlinear optical response at off-resonant conditions. Additionally, a search of effective optical limiters at 800 nm is useful for practical applications.

An interest in nanoparticle-containing films is caused due to their enhanced nonlinear optical response [23]. Such films have attracted interest due to their potential applications in optoelectronics as optical switches and optical limiters. The development of new thin film compounds containing both semiconductor and NPs allows for further enhancement of the nonlinear optical characteristics of such structures. During the last decade, there has been an interest in the nonlinear optical features of chalcogenide thin films [24−26]. The investigations of these films have shown their prospects as optical limiters.

Most of previous nonlinear optical studies of different materials in a strong electromagnetic field were performed using solutions and thick (of the order of a few micrometers) films. At the same time, it is interesting to investigate thin (of order of hundred nanometers) films. Particularly, gold nanocomposites have tremendous applications in various fields due to the influence of their SPR on the optical properties [27]. In the past decade, researchers have demonstrated the potential applications of Au NPs using different lasers [28, 29]. In those studies, the NPs were produced by laser ablation of the gold bulk targets. Laser ablation is an efficient method for the synthesis of NPs using different pulse durations, pulse energies, as well as various liquids. In most cases, the deionized water was used during the ablation to produce the gold NPs. Several studies have revealed variable nonlinear optical properties of Au NPs, nanorods, and thin films using different laser pulses [30−33]. Particularly, the optical nonlinearities of Au NPs arrays, which were determined by performing Z-scan measurements using a femtosecond laser (800 nm, 50 fs), were reported in [32]. The third-order nonlinear optical properties of Au NPs embedded in Al_2O_3, ZnO, and SiO_2 at the wavelength of 532 nm using the nanosecond Nd:YAG laser were analyzed in [33]. Previously, the high-order harmonics from Au NPs were studied in [34]. One can assume that the plasma produced on the thin films can enhance the efficiency of high-order harmonics due to the influence of NPs.

In this review, we discuss different nonlinear optical properties of silver and gold nanoparticles. Particularly, in Section 2 we analyze the nonlinear absorption and nonlinear refraction of Ag NPs aqueous solutions of different concentration, which were prepared by chemical reduction method. Z-scan measurements at different pulse durations (40 fs, 200 ps, and, in some cases, 5 ns) and wavelengths (800, 400, and 355 nm) are presented. We discuss the influence of different pulse repetition rate on the nonlinear optical characteristics. Additionally, we analyze the optical limiting and pump−probe studies of these NP solutions. In Section 3, we discuss the results of systematic studies of the ablation-produced Ag NPs prepared by 5 ns, 200 ps, and 60 fs pulses at the wavelengths of 1064 and 800 nm. We also discuss the OL in Ag NP suspension induced by 2PA and RSA at the wavelengths of 800 and 355 nm, respectively. We analyze the results of the nonlinear refraction and nonlinear absorption studies using different wavelengths and pulse durations of laser radiation. Third harmonic generation (THG) in the plasmas containing Ag NPs is analyzed. We also discuss the advantages in application of small (8 nm) Ag NPs for low- and high-order harmonic generation of ultrashort laser pulses. Overall, these studies show the correlation between strong nonlinear optical response of silver nanoparticles out of their SPR and efficient THG in the plasmas containing Ag NPs. In Section 4, we analyze the results of studying the optical, structural, and nonlinear optical characteristics of the Au NPs suspensions prepared using the chemical technique. A systematic study of the third-order optical nonlinearities of the Au NPs of four different sizes is discussed. We analyze the variable nonlinear optical response of these nanoparticles. We also discuss the optical limiting studies in Au NPs suspension. Finally, in Section 5, we discuss the third-order nonlinear optical properties and transient absorption of Au NPs thin film as well as analyze HHG from the ablated Au NP thin film.

2. INTERACTION OF PULSES OF DIFFERENT DURATION WITH CHEMICALLY PREPARED SILVER NANOPARTICLES: ANALYSIS OF OPTICAL NONLINEARITIES

There are a few reports on the variations of optical nonlinearities at different morphologies of Ag NPs [11, 35]. However, there are no systematic studies reported on the optical limiting, the influence of different concentrations of Ag NPs in liquids, and the effects of laser pulse duration, wavelength and repetition rate on their nonlinear optical properties. Below we discuss the interaction of pulses of different duration with chemically prepared silver nanoparticles and analyze their optical nonlinearities [36].

2.1. Experimental Arrangements

Ag NPs were synthesized by chemical reduction of sodium nitrate ($AgNO_3$) and sodium borohydride ($NaBH_4$). $AgNO_3$ and $NaBH_4$ were dissolved in deionized water respectively. The obtained $NaBH_4$ solution was placed under the conditions of ice water
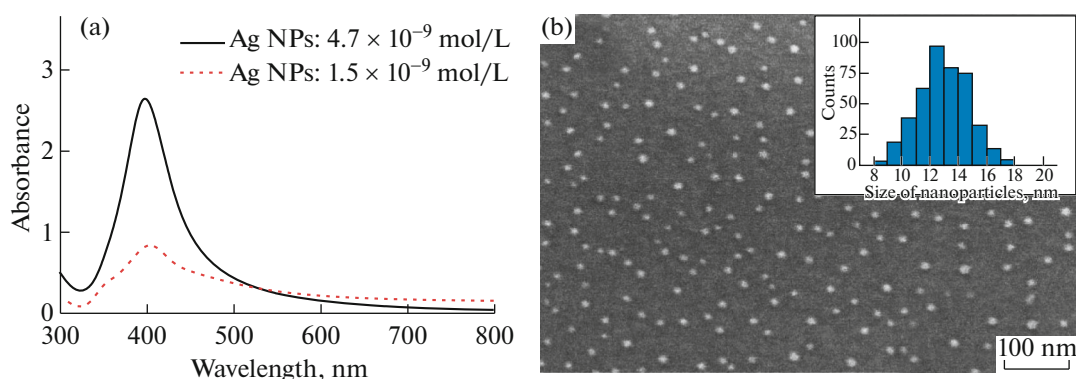
Fig. 1. (a) UV-visible absorption spectra of two Ag NPs solutions of different concentrations. (b) SEM image of Ag NPs and corresponding size distribution. Reproduced from [36] with permission from Hindawi.

bath (0°C) and stirred quickly. The $AgNO_3$ solution was trickled slowly and evenly into the $NaBH_4$ solution, allowing it to react fully under ice water bath. With the addition of $AgNO_3$, the solution gradually turned yellow, indicating that Ag NPs are formed. Ag NPs with different concentrations were obtained by adding different amount of $AgNO_3$ solution.

The absorption spectra of solutions at two concentrations are shown in Fig. 1a, which demonstrate the SPR absorption peaks at around 400 nm. In the case of the UV-visible spectral measurements, the 10 mm thick quartz cells were used. The intensities of absorption peaks were proportional to the concentrations of NPs. The morphology and particle size of Ag NPs were measured by scanning electron microscope (SEM) (S-4800, Hitachi). The NPs exhibited a regular spherical structure (Fig. 1b). The particle size distribution lied between 7 and 20 nm, with mean size of 13 nm. The concentrations (C) of two solutions of Ag NPs were calculated to be 1.5×10^{-9} and 4.7×10^{-9} mol/L.

Ti:sapphire laser (Spitfire Ace, Spectra-Physics) was used in these studies. It provided the 60 fs pulses at a wavelength of 800 nm and a repetition rate of 1 kHz. 10% of the output from the regenerative amplifier of this laser was separated prior to compressor stage from the main beam and used in different stages of these studies. The duration of these uncompressed pulses (200 ps) was measured by home-made autocorrelator. To study the effect of different wavelengths of probe pulses on the nonlinear optical characteristics of Ag NPs, the barium borate (BBO) crystal was used to convert 800 nm radiation to its second harmonic ($\lambda = 400$ nm).

The standard single beam Z-scan scheme was used for the measurements of the nonlinear optical properties of NPs using picosecond and femtosecond pulses. The transient absorption (TA) measurements of Ag NPs solutions were carried out by the pump–probe technique using 400 nm, 60 fs pulses. Laser pulse from

amplifier was split in the ratio of 30:70 with the use of beam splitter. The transmitted beam was used as a pump pulse and the reflected beam was used as a probe pulse. In the case of optical limiting experiments, the samples were installed in the focal plane.

2.2. Z-scan Measurements using Picosecond and Femtosecond Pulses

The 200 ps pulses were used for the open-aperture (OA) and closed-aperture (CA) Z-scans in the aqueous solutions of Ag NPs. The experimental results in the off-resonant case (800 nm) using 200 ps pulses are shown in Fig. 2. The theoretical fitting of experimental results was carried out, and these curves are shown in the corresponding figures. The nonlinear absorption coefficient was calculated to be 2×10^{-8} cm W^{-1}. At higher concentration of Ag NPs, the incident intensity was reduced by 15 times to 0.4×10^7 W cm^{-2}. The nonlinear absorption in that case was also induced by 2PA, while the nonlinear absorption coefficient (β) was increased by 15 times ($\beta = 3 \times 10^{-7}$ cm W^{-1}, Fig. 2d) compared with that of low concentration. The growth of nonlinear absorption coefficient is mainly caused by the increase of concentration. In the case of CA Z-scans, the nonlinear refractive index (γ) was increased by 10 times ($\gamma = 5 \times 10^{-13}$ and 5×10^{-12} cm^2 W^{-1} in the cases shown in Figs. 2a, 2b). Thus the nonlinear refractive index notably rises with the increase of concentration.

In the case of 400 nm, 200 ps pulses, the OA and CA Z-scans were similarly performed using two concentrations of NPs. At the conditions of higher concentration, the nonlinear absorption coefficient was two times larger compared to the low concentration case ($\beta = 1 \times 10^{-7}$ and 2×10^{-7} cm W^{-1}). The three-fold growth of the nonlinear refractive index for these two concentrations was observed (6×10^{-13} and 2×10^{-12} cm^2 W^{-1}).
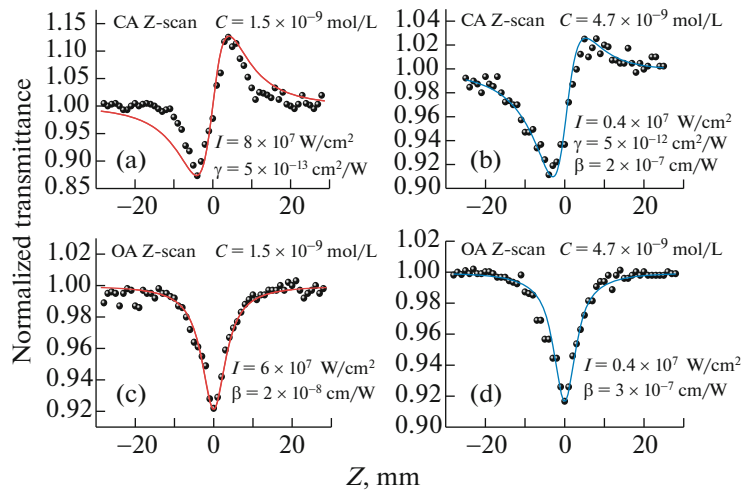
Fig. 2. Experimental results (spheres) and theoretical fittings (solid curves) of CA (a, b) and OA (c, d) Z-scans of the Ag NPs solutions of different concentrations ($C = 1.5 \times 10^{-9}$ mol/L (a, c), $C = 4.7 \times 10^{-9}$ mol/L (b, d)) using 800 nm, 200 ps laser pulses. Reproduced from [36] with permission from Hindawi.

A significant decrease of the nonlinear optical characteristics using 800 nm, 60 fs pulses compared with the case of using 200 ps probe pulses was observed. Under the same incident intensity (2×10^{11} W cm^{-2}), the increase of concentration led to a considerable growth of nonlinear absorption coefficient and nonlinear refractive index, similarly to the experiments using picosecond pulses. The growth rate of nonlinear refractive index was approximately the same as that of concentration ($\gamma = 3 \times 10^{-16}$ and 1×10^{-15} cm^2 W^{-1}). In the meantime, the nonlinear absorption coefficient was increased from 1.5×10^{-12} to 7×10^{-12} cm W^{-1}, i.e., almost 5 times, with the three-fold growth of NPs concentration.

The experimental results and theoretical fittings of the OA and CA Z- scans using shorter wavelength femtosecond pulses (400 nm, 60 fs) are shown in Fig. 3. Under these conditions, the OA and CA Z-scan curves were completely different from those observed in the case of 800 nm picosecond and femtosecond pulses, as well as 400 nm picosecond pulses. The OA Z-scans at two different concentrations of NPs showed the SA (Figs. 3a, 3b). The three-fold growth of concentration caused the two-fold increase of negative nonlinear absorption coefficient (-4×10^{-11} and -8×10^{-11} cm W^{-1}, Figs. 3c, 3d). The saturation intensities were calculated to be 2×10^{11} and 9×10^{10} W cm^{-2} for the low and high concentrations of Ag NPs.

The CA Z-scan curves showed the self-defocusing in studied samples (Figs. 3a, 3b). Similarly, the growth of NPs concentration led to the increase of nonlinear refractive index (-8×10^{-16} and -4×10^{-15} cm^2 W^{-1}). The analysis of experimental results using femtosecond pulses at the same concentration show that, at off-

resonant conditions ($\lambda = 800$ nm), the nonlinear absorption was attributed to 2PA, while in the resonant case ($\lambda = 400$ nm), it was caused by SA. The nonlinear refraction correspondingly transforms from the self-focusing in the case of above measurements to the self-defocusing in the case of 400 nm, 60 fs probe pulses. This peculiarity was maintained at both low and high concentrations of NPs.

In addition, the third harmonic of Nd:YAG nanosecond laser was used in this study. The OA Z-scan experiments using 355 nm, 5 ns, 10 Hz repetition rate pulses were carried out on the aqueous solution containing high concentration of Ag NPs under different incident intensities. The sample at these conditions showed SA, and the growth of incident intensity led to the enhancement of positive nonlinear absorption leading to the prevailing dominance of RSA.

The large difference in the nonlinearities of NPs can be caused by involvement of different nonlinear optical processes. In particular, the role of saturable and reverse saturable absorption can be largely enhanced at the conditions when the relaxation time constants of excited states participating in those processes become larger compared with short laser pulses. At those conditions, longer (picosecond) probe pulses can cause larger nonlinear optical response compared with femtosecond pulses. To determine the relaxation time constants, the pump−probe transient absorption studies of samples were carried out.

2.3. Pump−Probe Measurements of Transient Absorption and Optical Limiting

TA measurements for chemically synthesized Ag NPs ($C = 4.7 \times 10^{-9}$ mol/L) were performed using noncollinear degenerate pump−probe spectroscopy
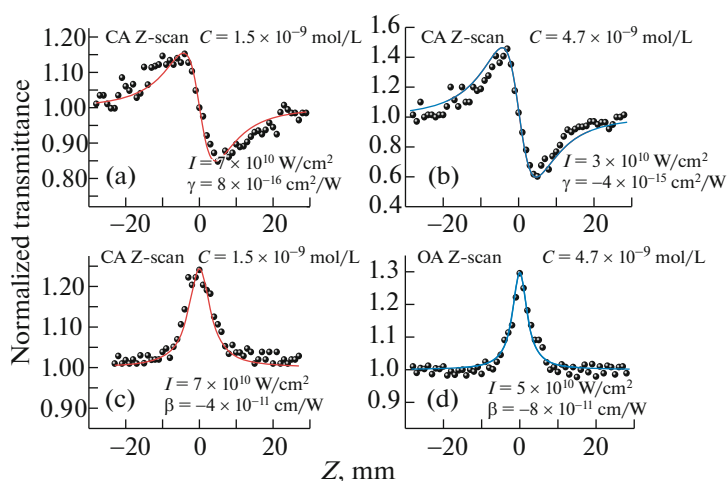
Fig. 3. Experimental results and theoretical fittings of CA and OA Z-scans of the Ag NPs solutions of different concentrations using 400 nm, 60 fs pulses. Reproduced from [36] with permission from Hindawi.
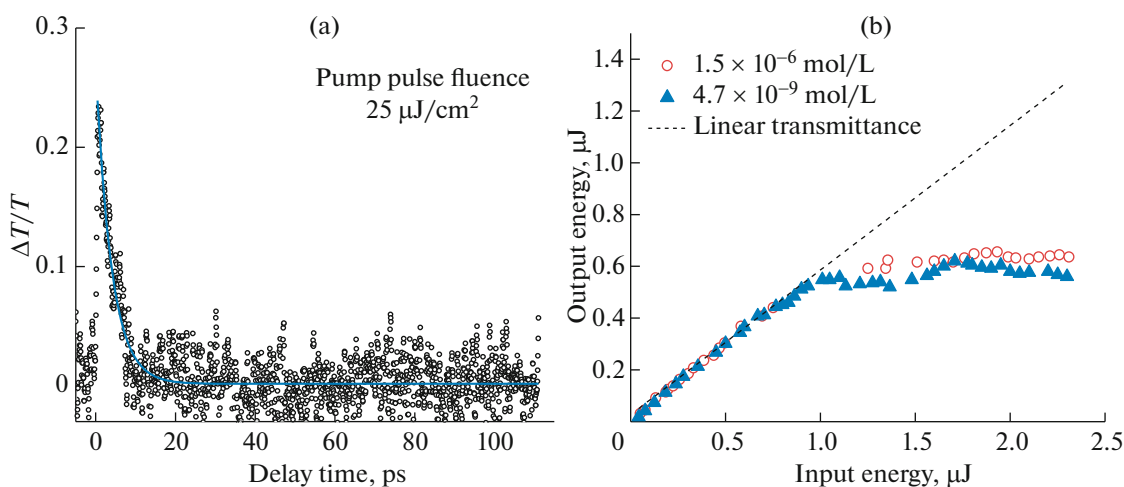

Fig. 4. (a) Transient absorption profile with respect to delay time in the case of 400 nm laser pulses. Scattered empty circles show the experimental measurements and the solid line represents the single exponential fit to the experimental data. (b) Optical limiting of 800 nm, 60 fs pulses using Ag NPs solutions at low ($C = 1.5 \times 10^{-9}$ mol/L, empty circles) and high ($C = 4.7 \times 10^{-9}$ mol/L, filled triangles) concentrations. Reproduced from [36] with permission from Hindawi.

(400 nm, 60 fs pulses). Figure 4a represents the TA profile of Ag NPs in deionized water measured using the femtosecond pump pulse fluence of 25 μJ/cm². Prior to TA study of Ag NP, TA profile for water was also measured, which showed no change in transmittance of the probe pulse at the maximum fluence used in this experiment (100 μJ/cm²). TA profile was compared with the single exponential fit to determine the relaxation time constant, which was measured to be $\tau_1 = 3.9$ ps at the pump pulse fluence of 25 μJ/cm². This parameters is significantly larger compared with the pulse duration of used femtosecond pulses. In the case of Ag NPs, excitation generally happens through plasmon excitation where the electron–electron scat-

tering time scale is of the order of few femtoseconds, whereas the electron–phonon interaction lasts much longer time with the time scale of a few picosecond [37]. The femtosecond dynamics associated to the electron–electron scattering in Ag NPs was not observed in the TA profile, which can be explained by faster electron–electron scattering dynamics compared to the employed laser pulse width. The electron–phonon interaction in Ag NPs generally occurs in 100 fs to ps time scale hence the time constant of 3.9 ps can directly be attributed to the electron–phonon interaction at 400 nm.

Optical limiting is generally analyzed using nanosecond pulses. Meanwhile, femtosecond pulses can

Table 1. Nonlinear optical parameters of Ag NPs solutions. Reproduced from [36] with permission from Hindawi

	$C = 1.5 \times 10^{-9}$ mol/L				$C = 4.7 \times 10^{-9}$ mol/L			
	800 nm		400 nm		800 nm		400 nm	
	ps	fs	ps	fs	ps	fs	ps	fs
γ, cm^2 W^{-1}	5×10^{-13}	3×10^{-16}	6×10^{-13}	-8×10^{-16}	5×10^{-12}	1×10^{-15}	2×10^{-12}	-4×10^{-15}
β_{2PA}, cm W^{-1}	2×10^{-8}		1×10^{-7}		3×10^{-7}		2×10^{-7}	
β_{RSA}, cm W^{-1}		1.5×10^{-12}				7×10^{-12}		
β_{SA}, cm W^{-1}				-4×10^{-11}				-8×10^{-11}
I_{sat}, W cm^{-2}				2×10^{11}				9×10^{10}
τ_1, ps								3.9
E_{OL}, μJ		0.6				0.5		

effectively avoid heat accumulation and other effects compared with nanosecond pulses. Below we discuss this process in the case of femtosecond pulses. Figure 4b demonstrates the optical limiting in the Ag NPs solutions at two concentrations in the case of 800 nm, 60 fs radiation. As it is shown in the figure, the transmitted energy increases linearly with the growth of the incident pulse energy in the low energy range and then reaches the saturation.

The transmitted energy approaches to a steady value when the incident energy of 800 nm pulses increased above 0.75 μJ. The optical limiting threshold was defined as the maximum transmitted energies $E_{OL} = 0.5$ μJ and $E_{OL} = 0.6$ μJ in the case of high and low concentrations of NPs, respectively. One can see that this parameter decreases with the growth of Ag NPs concentration.

All measured nonlinear optical parameters are collected in Table 1, where the γ, β_{2PA}, β_{RSA}, β_{SA}, I_{sat}, τ_1, and E_{OL} for two concentrations of NPs and two wavelengths (800 and 400 nm) are shown.

3. STRONG THIRD-ORDER OPTICAL NONLINEARITIES OF AG NANOPARTICLES SYNTHESIZED BY LASER ABLATION OF BULK SILVER IN WATER AND AIR

No systematic studies, which combine the analysis of nonlinear absorption/refraction and lowest order harmonic generation in the same nanoparticle medium, were reported so far. Earlier studies were focused on the particular properties of Ag NPs related with different components of their third-order nonlinear susceptibilities. Particularly, nobody studied in depth the correlation between different components of those susceptibilities. Here we analyze those groups of studies to demonstrate the fact that exceptionally strong nonlinearities (particularly, nonlinear absorption) out of the SPRs of nanoparticles strongly correlate with highly efficient third harmonic generation

in Ag NPs. These studies show the way to explain the earlier reported exceptionally strong HHG conversion efficiency in Ag NP plasma by the specific properties of those particles related with involvement of their plasmonic properties in the enhancement of nonlinear optical response in the extreme ultraviolet range [38].

The Ag NPs were synthesized by ablation of bulk silver in water using nanosecond laser (Q-Smart 850, Coherent). Laser radiation (wavelength: 1064 nm, pulse duration: 5 ns, pulse repetition rate: 10 Hz, pulse energy: 40 mJ) was focused by 100 mm focal length lens on the surface of silver target immersed in deionized water. The target sizes were $5 \times 5 \times 2$ mm. The ablation was carried out during 30 min. The color of suspension was changed during laser ablation until became yellow shade. The silver target was also ablated using 200 ps, 800 nm and 60 fs, 800 nm laser pulses.

The nonlinear optical parameters of Ag NP suspension were investigated using Z-scan technique. The nonlinear optical studies of Ag NP suspensions were carried out using nanosecond and femtosecond laser pulses at four different wavelengths (1064, 800, 400, and 355 nm). The OL study was carried out by varying the energy of the pulses propagating through the quartz cell containing Ag NP suspension, which was installed in the focal plane. A noncollinear degenerate pump−probe technique was applied to study the transient absorption in Ag NPs. In the case of THG studies the laser radiation ($\lambda = 800$ nm, $\tau = 60$ fs) was focused by a 400 mm focal length lens on the LPP. The beam waist radius of the focused radiation was 38 μm. The spectral characteristics of third harmonic radiation ($\lambda = 266$ nm) were analyzed by a spectrometer (USB2000, Ocean Optics). To create plasma plume, a pulse was split from the Ti:sapphire laser by a beamsplitter before the compression of fundamental uncompressed pulse. The heating pulse duration was 210 ps. This radiation was focused on the target to heat it and produce LPP in the air conditions. A delay
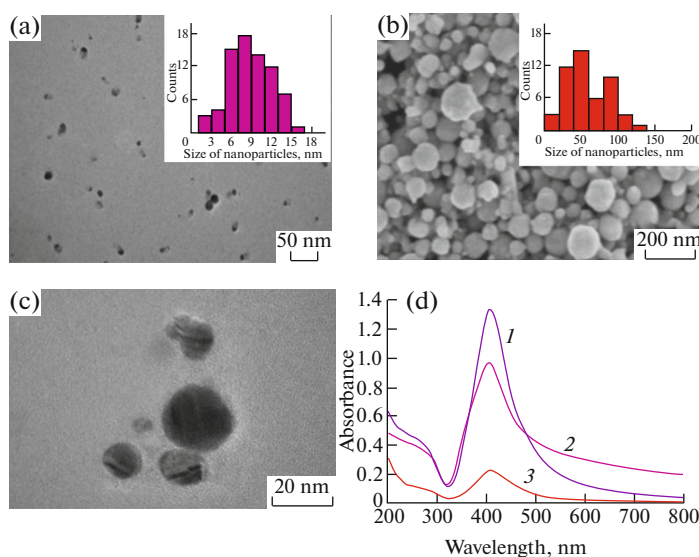
Fig. 5. (a) TEM image and histogram of size distribution of Ag NPs in the case of ablation in water using 1064 nm, 5 ns pulses, (b) SEM image and size distribution of Ag NPs ablated in water using 800 nm, 200 ps pulses, (c) TEM image of Ag NPs in the case of ablation in water using 800 nm, 60 fs pulses. (d) Absorption spectra of Ag NPs suspensions in case of ablation using (*1*) 1064 nm, 5 ns, (*2*) 800 nm, 200 ps, and (*3*) 800 nm, 60 fs pulses. Reproduced from [38] with permission from Springer.

between fundamental and heating pulses was adjusted to be 38 ns.

TEM and SEM images and histograms of the Ag NPs prepared by ablation of bulk silver using pulses of different duration are presented in Figs. 5a, 5b, 5c. The linear absorption spectra of Ag NP suspensions (Fig. 5d) were measured using a spectrophotometer (Agilent Technologies). The SPRs of Ag NPs in two cases of ablation were observed at 402 nm. In the case of picosecond ablation the linear absorption coefficient of Ag NPs at $\lambda > 450$ nm was larger compared to the case of nanosecond ablation. The sizes of NPs were measured to be 8 and 50 nm, by using the 5 ns and 210 ps pulses for laser ablation.

3.1. Optical Limiting and Third-order Nonlinearities of Ag NP Suspension

Optical limiting is the important aspect for the application of nanostructured materials in nonlinear optics and laser physics particularly to protect sensitive systems and eyes from high-power laser radiation [39]. Earlier the optical limiting using Ag NPs was reported in [40]. It was shown that OL in these NPs in the field of nanosecond laser pulses at $\lambda = 532$ nm is much stronger than in other materials such as C_{60} and chloroaluminumphthalocyanine. Below we analyze OL using 800 nm, 60 fs, and 355 nm, 5 ns laser pulses, which propagated through the suspension of Ag NPs in deionized water. The suspension was obtained during ablation of bulk silver using nanosecond laser pulses. This suspension was placed at the focal plane of 400 mm focal length lens.

The linear dependence between input and output 800 nm, 60 fs pulses was maintained up to the input pulse energy of ~0.6 μJ (Fig. 6a, filled triangles). Further growth of input pulse energy led to OL of propagated laser radiation due to 2PA. This process was maintained up to the energy of 800 nm pulses of ~2.0 μJ, which allowed stabilization of output energy at the level of 0.5 μJ along the 0.6−2.2 μJ energy range of input pulses. The OL in pure water was also studied in this energy range of propagated laser pulses. The slope of linear fitting for pure deionized water at small input pulse energies was equal to 1.0, while the slope of linear fitting of Ag NPs was equal to 0.7. The latter slope was corresponded to the initial transmittance of the suspension containing Ag NPs in deionized water. In the case of water, the inclination of I_{out}/I_{in} from the linear dependence was also observed due to white light generation (Fig. 4a, empty circles).

In the case of nanosecond laser pulses RSA led to the OL of 355 nm laser radiation. This process was analyzed in the range of energies between 150 to 600 μJ (Fig. 6b). One can see that Ag NP suspension demonstrated excellent OL properties in the case of nanosecond UV pulses. Those observations of the optical limiting in silver nanoparticles suspension were attributed to 2PA and RSA at the wavelengths of 800 nm and 355 nm probe pulses, respectively. During these experiments, the OL was analyzed by either increasing or decreasing the energy of laser pulses. In these two cases, the similarities with the same threshold energy for OL were obtained.

The nonlinear optical parameters of Ag NP suspensions measured at different experimental condi-
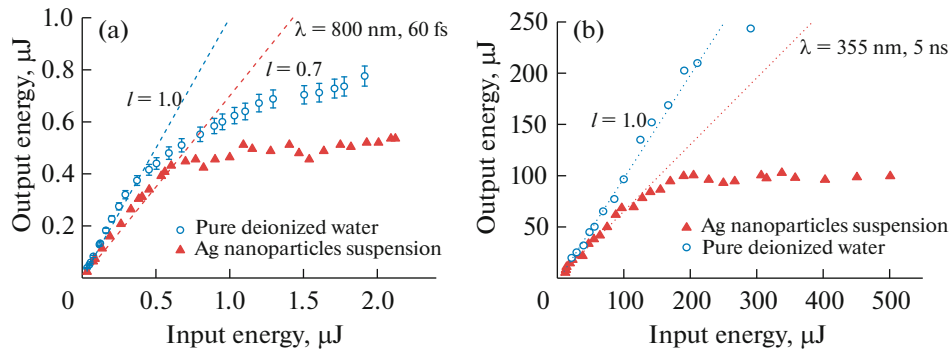
Fig. 6. Optical limiting in the aqueous suspension of Ag NPs (filled triangles) and pure water (empty circles) using (a) 60 fs, 800 nm, and (b) 5 ns, 355 nm probe pulses. Dotted lines show the linear dependences between output and input pulse energies at the lower energy ranges of input pulses. Reproduced from [38] with permission from Springer.

tions are collected in Table 2. The concentration of Ag NPs in the case of femtosecond ablation was notably smaller than concentration of the NPs produced during ablation using picosecond and nanosecond pulses due to less efficient ablation in the former case. Because of this the nonlinear optical response of these species under action of nanosecond probe pulses was at the threshold of registration.

The actual values of the nonlinear susceptibilities of NPs are considerably larger than those of NP suspensions due to small fraction of nanoparticles in the whole volume of solvent. A simple and well-established method for estimation of the nonlinear suscep-

tibilities of nanoparticles is to divide the nonlinear susceptibility of compound by the volume or weight part of NPs. In fact, the third-order nonlinear susceptibilities [$\chi^{(3)}$] of composites, and correspondingly, γ and β, are also depend on the local field factor as

$$\chi^{(3)} = p|f|^2 f^2 \chi^{(3)}_{NPs}. \tag{1}$$

Here, $\chi^{(3)}_{NPs}$ is the third-order nonlinear susceptibility of NPs, f is the local field factor, and p is the filling factor (i.e., volume or weight part). The enhancement due to local field factor is insignificant in the case of metal NPs far from their SPRs. In particular, the

Table 2. Nonlinear optical parameters of Ag NP suspensions. Reproduced from [38] with permission from Springer

		Ag NPs (8 nm)	Ag NPs (50 nm)	Ag NPs (15 nm)
		Parameters of heating pulses		
		$\lambda = 1064$ nm, $\tau = 5$ ns	$\lambda = 800$ nm, $\tau = 200$ ps	$\lambda = 800$ nm, $\tau = 60$ fs
800 nm, 60 fs	γ, cm^2 W^{-1}	2.0×10^{-15}	3.4×10^{-15}	1.9×10^{-15}
	β_{2PA}, cm W^{-1}	1.0×10^{-10}	0.9×10^{-10}	0.9×10^{-10}
	$\chi^{(3)}$, esu units	1.8×10^{-9}	2.6×10^{-9}	1.6×10^{-9}
400 nm, 60 fs	γ, cm^2 W^{-1}	2.1×10^{-15}	1.5×10^{-15}	3.2×10^{-15}
	β, cm W^{-1}	RSA: 8.6×10^{-10}	RSA: 5.5×10^{-10}	2PA: 5.5×10^{-10}
	β_{SA}, cm W^{-1}	1.9×10^{-10}	–	–
	$\chi^{(3)}$, esu units	3.6×10^{-9}	2.8×10^{-9}	3.3×10^{-9}
1064 nm, 5 ns	γ, cm^2 W^{-1}	-1.2×10^{-14}	–	–
	β_{2PA}, cm W^{-1}	3.0×10^{-10}	–	–
	$\chi^{(3)}$, esu units	0.6×10^{-9}	–	–
355 nm, 5 ns	γ, cm^2 W^{-1}	–	-2.5×10^{-15}	–
	β_{RSA}, cm W^{-1}	2.0×10^{-10}	9.0×10^{-10}	–
	β_{SA}, cm W^{-1}	-3.0×10^{-11}	–	–
	γ, cm^2 W^{-1}	-0.2×10^{-9}	0.8×10^{-9}	–

insignificant enhancement of local field factor for Mn nanoparticles suspension was reported in [41]. In the case of Ag NPs $|f|^2$ is in the range of 0.1 and 1 in non-resonance conditions (i.e., at the wavelengths of 800, 1064, and 355 nm). In the resonance conditions the local field factor increases becomes equal to 3.6 at 400 nm. The f of small-sized Ag NPs at different wavelengths was estimated in [42] where the influence of the local field factor on the power of probe pulse, particle size and photon energy around the SPR was analyzed.

Third-order nonlinear susceptibilities in media having nonlinear absorption and refractive index can be considered to be a complex quantity

$$\chi^{(3)} = \operatorname{Re}\chi^{(3)} + i\operatorname{Im}\chi^{(3)}, \tag{2}$$

where the imaginary part is related to the nonlinear absorption coefficient through

$$\operatorname{Im}\chi^{(3)} = \frac{n^2\varepsilon_0 c\lambda\beta}{2\pi}, \tag{3}$$

and the real part is related to γ through

$$\operatorname{Re}\chi^{(3)} = 2n^2\varepsilon_0 c\gamma. \tag{4}$$

Here, ε_0 is the permittivity of free space. For the presentation of $\chi^{(3)}$ in esu units, one can use the relation $\chi^{(3)}$ [esu units] $= (9\times10^8/4\pi)\chi^{(3)}$ [SI units]. $\chi^{(3)}$ of NP suspensions was calculated and included in Table 2.

The parameters shown in Table 2 are attributed to the suspensions of Ag NPs. The estimates show that the volume fraction of NPs in suspensions was in the range of 10^{-3}. The values of γ and β of Ag NPs with 8 nm sizes can be multiplied by a factor of 1.0×10^5 for 1064 nm (i.e., far from SPR) and 11.0 for 400 nm pulses (i.e., in the resonance conditions) to determine these parameters attributed to Ag NPs taking into account the f defined from [42]. In particular, β of suspension measured by 1064 nm, 5 ns and 400 nm, 60 fs probe pulses was measured to be 3.0×10^{-10} cm W^{-1}, and 8.6×10^{-10} cm W^{-1}. One can estimate β of NPs at these conditions to be 3.0×10^{-5}, and 9.4×10^{-9} cm W^{-1}, respectively.

3.2. Transient Absorption Measurements

Figure 7 shows the pump–probe data for 8 nm Ag NPs prepared by ablation using nanosecond pulses in deionized water. The TA curve for Ag NPs in water was fitted with single exponential fit (solid curve). The profile of pump–probe signal of Ag NPs in deionized water indicates the process of photo-bleaching due to the resonant excitation at 400 nm. The lifetime of excited plasmon for Ag NPs at 400 nm was measured to be 2.5 ps, which can be assigned to the electron–phonon relaxation time. The theoretical approaches for calculating the ultrafast nonlinear optical
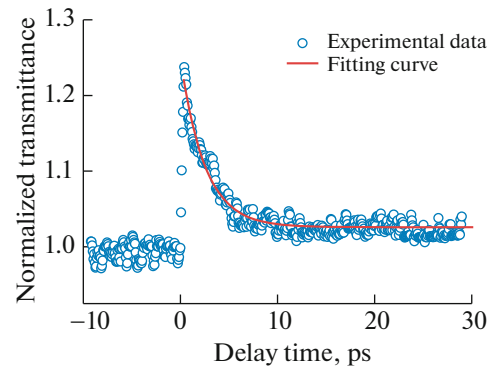

Fig. 7. Pump–probe measurements of Ag NP suspension at the wavelength of 400 nm using 60 fs laser pulses. Reproduced from [38] with permission from Springer.

responses of dielectric composite materials consisting of metal nanoparticles with different sizes and shapes are described in [43, 44]. For particles with smaller sizes the relaxation process due to electron–phonon interaction is faster than for particles with larger sizes. It was shown that red shift of the peaks of the SPR related to increase of Ag NPs sizes led to the change of the nonlinear absorption in the field of femtosecond laser pulses.

For understanding the dynamics of electron relaxation in excited Ag NPs at resonance conditions the Z-scan and pump–probe data were used. One can determine the cross-section of bleaching of the Ag NPs by equation [45]:

$$\sigma_{12} = h\nu/(2I_{\text{sat}}\tau_{21}). \tag{5}$$

Where σ_{12} is the absorption cross section of Ag NPs and τ_{21} is the relaxation time of electron–phonon interaction. Using this equation and values of saturation intensities $I_{\text{sat}} = 6.3 \times 10^8$ W cm^{-2} at 355 nm, 5 ns and $I_{\text{sat}} = 2.4 \times 10^{10}$ W cm^{-2} at 400 nm, 60 fs probe pulses the excited state absorption cross sections at the wavelengths of 355 and 400 nm were calculated as 6.7×10^{-16} and 8×10^{-17} cm^2, respectively.

3.3. Third Harmonic Generation in Laser-Produced Plasmas Containing Ag NPs

Prior to the THG studies the structural and optical properties of deposited thin films on the surfaces of quartz and silicon substrates were analyzed to proof the presence of Ag NPs during ablation of silver target in air. The absorption spectrum of the deposited thin films showed the appearance of SPR at 415 nm due to formation of Ag NPs. The atomic force microscopy of the deposited silver films showed broad distribution of NPs' sizes. The theoretical analysis also showed that small sized Ag NPs started to evaporate 80 ps from the beginning of irradiating the bulk silver target using 200 ps, 800 nm pulses. Different factors limiting THG
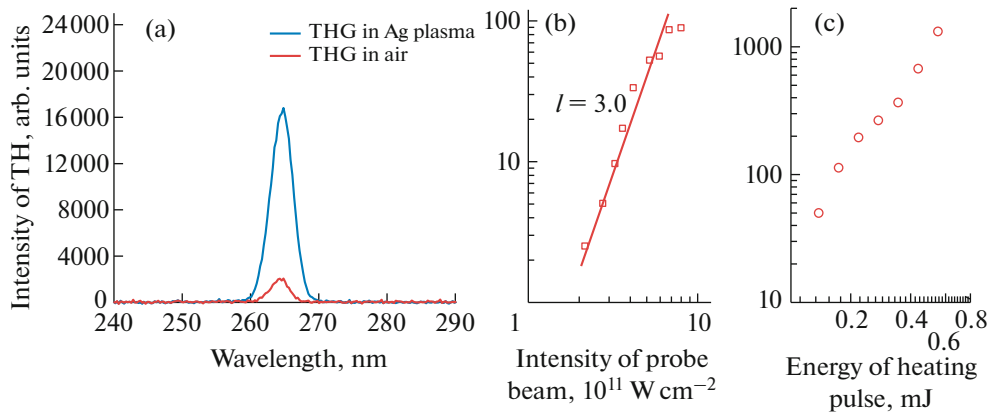
Fig. 8. (a) Spectra of the third harmonic generation in the plasma containing Ag NPs (thick curve) and in the air (thin curve). (b) Dependence of the intensity of TH on the intensity of femtosecond laser pulses in silver plasma. (c) Dependence of the intensity of TH on the energy of heating picosecond laser pulses. Reproduced from [38] with permission from Springer.

in plasmas was analyzed in [46]. This type of ablation facilitates condensation of metal atoms into clusters and rapid growth of the atomic clusters into nanoparticles with maximum sizes barely exceeding 10 nm. The NPs with large sizes at around 100 nm did not contribute to low-order harmonic process. The velocity of nanoparticles depends on the mass and fluence of heating beam. Only small clusters appear in the area of interaction at the moment of femtosecond pulse arrival (i.e., 38 ns from the beginning of ablation). Thus these species are responsible for harmonic generation in present conditions.

In discussed studies, the advantages in application of small Ag NPs for low-order harmonic generation of femtosecond laser pulses. Some previous studies using the atomic plasmas produced on the surfaces of bulk silver target and the plasmas containing Ag NPs have shown relatively high conversion efficiency of harmonics generated in such media [47]. The usefulness in application Ag NPs for enhancement of HHG in the extreme ultraviolet range has also been demonstrated in [48].

Figure 8 presents the spectra and the intensity of the third harmonic (TH) as a function of the probe and the heating pulse intensity in the plasma plumes containing Ag NPs. One can see a six fold enhancement of TH efficiency in the case of air conditions compared with the THG in air. We also analyze the TH yield at the air pressure of 1.3 kPa. In this case the $20\times$ enhancement of TH yield from Ag plasma with regard to residual air was obtained. A slope of fitting line in Fig. 8b corresponds to 3, which is the indication of the expected cubic dependence between fundamental and harmonic pulses in the case of THG. Figure 8c shows the dependence of TH yield on the heating pulse energy. No saturation of THG at the highest used energy of heating picosecond pulses (0.5 mJ) was observed.

The conversion towards 266 nm radiation in the case of plasma plume was notably stronger compared with THG in air. THG conversion efficiencies in air and Ag NP plasmas were determined to be 1×10^{-3} and 4×10^{-3} in the case of 800 nm, 60 fs driving pulses. The value of conversion efficiency in air was comparable with earlier reported study carried out at similar conditions [49].

4. SIZE-DEPENDENT OFF-RESONANT NONLINEAR OPTICAL PROPERTIES OF GOLD NANOPARTICLES AND DEMONSTRATION OF EFFICIENT OPTICAL LIMITING

The enhanced nonlinear optical properties of nanoparticles as compared to those of the bulk state make nanoscale particles more promising for designing optoelectronic and micro-electronic devices. In this connection, the growing interest in gold nanoparticles is related to their unique optical, morphological, and electronic properties that are based on the quantum-confinement effect [50]. Many types of studies for Au NPs with different shapes (sphere, cube, octahedron, rod, etc.) have been carried out [51–57]. The theoretical models have brought forward an understanding of the origin of these fascinating phenomena in Au NPs [58].

Above analysis presented in Introduction section shows that the optical nonlinearities of Au NPs under 530 nm resonant conditions have been studied extensively. Meanwhile, the analysis of the off-resonant nonlinear optical behavior of synthesized Au NPs of different sizes at around 800 and 400 nm or even shorter wavelengths is of special importance. Some variations of the third-order nonlinear properties in Au NPs have been found for wavelengths at around 800 nm [58]. Meanwhile, the role of spatial characteristics of nanoparticles at off-resonant conditions yet
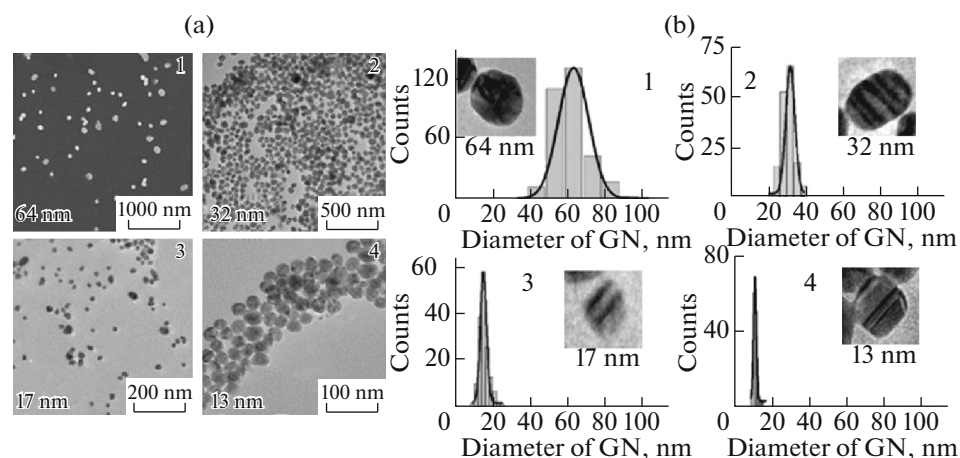
Fig. 9. (a) SEM image of (1) 64 nm Au NPs. TEM images of (2) 32, (3) 17, and (4) 13 nm Au NPs. (b) Histograms of corresponding nanoparticles and images of single gold nanoparticles (GN). Reproduced from [59] with permission from Optical Society of America.

took attention during previous studies of Au NPs. The size dependent variations of nonlinear optical characteristics along with the strong nonlinear optical absorption of both large (>50 nm) and small (<20 nm) Au NPs under 400 and 800 nm femtosecond pulses can be used for different applications, such as high-order harmonic generation in "optimally" prepared Au NPs plasmas, optical limiting and switching, etc.

Below we analyze the results of studying the optical, structural, and nonlinear optical characteristics of the Au NPs suspensions prepared using the chemical technique [59]. A systematic study of the third-order optical nonlinearities of the Au NPs of four different sizes is discussed. We analyze the variable nonlinear optical response of these nanoparticles. We also discuss the optical limiting studies in Au NPs suspension.

4.1. Synthesis and Characterization of Au NPs Suspensions

Gold nanoparticles can be synthesized by different methods. Since the optical, and especially nonlinear optical, properties are strongly governed by Au NPs sizes, morphology, and surrounding environment, a modified preparation of the Turkevich citrate method [60] was chosen for the synthesis of four different sizes of nanoparticles. The sizes of the Au NPs were controlled by quantitatively varying the addition of the trisodium citrate (stabilising and reducing agent) to tetrachloroauric acid.

Au NPs were prepared by the reduction of tetrachloroauric acid ($HAuCl_4$) with trisodium citrate ($Na_3C_6H_5O_7$). The $HAuCl_4$ solution (1% 2 mL) and deionised water (48 mL) were heated until boiling. Then specific quantities of trisodium citrate along with deionized water (5 mL) were added quickly into this boiling mixture under vigorous stirring. The solu-

tion turned from yellow to wine-red color and then the heating was stopped after 15 minutes. The stirring was continued for another 30 minutes until the reaction mixture was cooled down. To prepare the Au NPs suspensions of different sizes, 0.0143, 0.0285, 0.114, and 0.228 g of trisodium citrate were added during the process to stabilize and reduce the $HAuCl_4$ and to obtain a descending size distribution of Au NPs. The particle size and the shape of prepared samples were determined using a scanning electron microscope (SEM, S-4800, Hitachi) and a transmission electron microscope (TEM, JEM 2100F, JEOL). The absorption measurements of samples were performed using a UV-Vis spectrophotometer (Cary Series, Agilent Technologies). The optical spectra were measured in the range of 400 to 800 nm to detect the characteristic SPR and visible light absorption of Au NPs suspensions. The conventional Z-scan scheme was used to study the off-resonant third-order nonlinear optical properties of Au NPs suspensions.

The particle size distribution and the morphology of synthesized Au NPs were determined from the SEM and TEM images (Fig. 9a). The mean diameters of Au NPs were found to be 64, 32, 17, and 13 nm in the case of addition of different amount of trisodium citrate to the mixture. It was distinctly observed that the increase of trisodium citrate led to a decrease of Au NPs sizes, which has shown that the relative concentration of the precursor and the reducing agent strongly affect the nucleation and the growth progression of Au NPs. For particles below 20 nm, the size distribution was comparatively homogeneous and the standard deviation from mean size was minimal. Electron microscopy of suspensions (Fig. 9b) demonstrated no changes in the size parameters of the nanoparticles occurring during two months period.
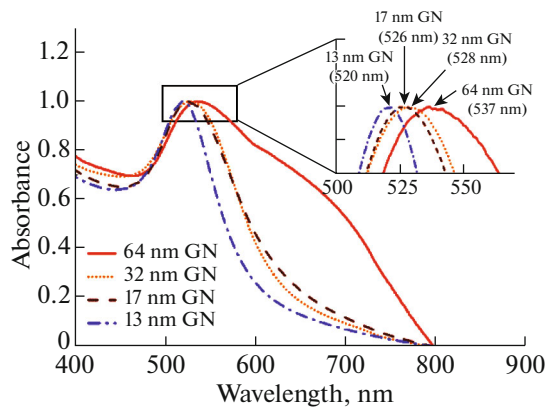
Fig. 10. Absorption spectra of different Au NPs. Inset shows the enlarged area of the maximums of the SPR of different Au NPs. Reproduced from [59] with permission from Optical Society of America.

The size distribution of Au NPs remained stable as well.

The optical properties of Au NPs show the characteristic absorption dominated by SPR peaks at 537, 528, 526, and 521 nm for particle sizes of 64, 32, 17, and 13 nm, respectively (Fig. 10). For the metal nanoparticles, the size controllability and surface tenability are essential. The electronic and optical properties exploited in their applications are highly dependent on the particle size and shape. The red shift is also accompanied by a broadening of the SPR band. The red shift increased with the increase in particle size and is characterized by appearance of blue colored solution. The absorption spectrum is determined by the localized surface plasmon resonance of the metal nanoparticles in the suspension [61]. The broad range of particle sizes and shape distributions for 64 nm Au NPs resulted in a notably broader absorption spectrum. The width and position of SPR was varied as a function of particle size and shape (see inset in Fig. 10).

As has been previously pointed out in a number of studies, the absorption spectra of Au NPs can be controlled, to a considerable extent, by the parameters and methods of preparation of the nanoparticle-contained solutions. The positions of the SPR of these colloidal suspensions prepared by chemical methods correspond to the range of 530−550 nm, whereas, in the case of laser ablation, the peak of the SPR is slightly shifted toward shorter wavelengths due to the influence of small-sized particles. Variations of the absorption spectra of the chemically prepared Au NPs were analyzed during two months and no significant changes were observed.

Previously, the aggregation and precipitation of Au NPs were the main reasons for variation of the optical and nonlinear optical properties of the nanoparticle suspensions obtained by chemical and laser ablation

methods. Note that the nonlinear optical studies described in this paper were performed at the conditions of the stabilization of the size and spectral characteristics of the Au NPs in the suspensions. The studies were carried out in the spectral regions corresponding to single (in the case of 400 nm radiation) and two-photon (in the case of 800 nm radiation) absorption in the suspensions containing Au NPs. These nanoparticles showed mostly spherical shape. Notice that the absorption peak at around 527 nm corresponds to a commonly reported SPR of the spherical Au NPs.

Once the sizes of nanoparticles increase, their peak of plasmon resonance will be tuned towards longer wavelength and vice versa. One can use Mie and Drude theory to show that the sizes of Au NPs can be calculated from their absorption spectra. The bandwidth of SPR has earlier been used [62] to estimate Au NPs sizes according to the equation

$$\Delta\omega_{1/2} = v_F/R, \qquad (6)$$

where $\Delta\omega_{1/2}$ is the half width of the absorption band, R is the Au NPs radius in nanometers, and F is the Fermi velocity of conduction electrons in gold (1.39×10^{15} nm/s). By applying this formula, which is useful for small particles ($R < 20$ nm), the diameter of Au NPs in studied suspension was estimated (11 nm). This value is close to the direct measurements of the mean size of Au NPs using the TEM images (13 nm).

4.2. Nonlinear Optical Studies

The main nonlinear optical process observed using OA scheme at $\lambda = 800$ nm and related to the small-sized Au NPs was the nonlinear absorption (Fig. 11a). This process has earlier been associated with the RSA [60]. These OA Z-scans were obtained in the case of the suspensions containing 13, 17, and 32 nm nanoparticles. The values of the nonlinear absorption coefficients for these three Au NPs suspensions were calculated to be 1.5×10^{-12}, 1.5×10^{-12}, and 2×10^{-12} cm W^{-1}, respectively. The nonlinear absorption in these suspensions was also observed in the case of 400 nm pulses. In this case the process was also attributed to RSA (Fig. 11b). The measured values of the nonlinear absorption coefficients attributed to RSA in these three Au NPs suspensions were 1×10^{-11}, 1.5×10^{-11}, and 1.2×10^{-11} cm W^{-1}, respectively, which are larger than in the case of longer wavelength pulses. No effect of the fused silica cell and water was observed up to $I_0 = 3 \times 10^{11}$ W cm^{-2}.

In the meantime, the SA was observed in the case of the suspension containing 64 nm Au NPs by using both 800 and 400 nm pulses. Though the SA in the case of 800 nm pulses was relatively weak ($|\Delta T| \leq 0.075$, Fig. 11a, upper curve), its influence was notably increased in the case of shorter wavelength (400 nm) pulses ($|\Delta T| \sim 0.2$, Fig. 11b, upper curve) even at significantly smaller intensity. This wavelength-depen-
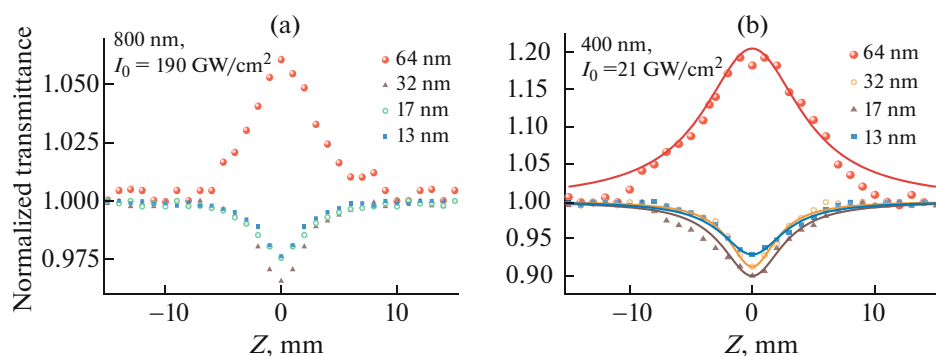
Fig. 11. OA Z-scans of suspensions containing different Au NPs using (a) 800 and (b) 400 nm, 40 fs pulses at the intensities of 1.9×10^{11} and 4.5×10^{10} W cm^{-2} in the focal plane. Reproduced from [59] with permission from Optical Society of America.

dent growth of SA is a commonly observed feature attributed to larger cross section of population of the excited states responsible for RSA in the case of shorter wavelength excitation.

The electric field polarizing a nanoparticle may substantially exceed the external applied field. The most remarkable manifestation of this effect is related to the plasmonic properties, which enhance the non-linear optical characteristics of the medium in the vicinity of the central wavelength of SPR, especially in the case of resonant excitation. This resonance can be considered in the framework of the model of collective oscillations of surface electrons in a nanoparticle. However, in the used case (800 and 400 nm pulses) the excitation occurs far from the SPR band of Au NPs (~530 nm). Thus the SA of Au NPs hardly could be attributed only to the influence of SPR, which is the coherent coupling between free electrons of the conduction band and the external electromagnetic field emitting at approximately similar wavelength [63].

The measurements and calculations of nonlinear refractive indices of Au NPs suspensions were carried out using the standard CA Z-scans and fitting procedures. The γ at two wavelengths were calculated

to be $\gamma_{800\,nm} = 1.4 \times 10^{-11}$ cm^2 W^{-1} and $\gamma_{400\,nm} = 2 \times 10^{-10}$ cm^2 W^{-1} (both for 17 nm Au NPs suspension). The calculated data of the nonlinear optical characteristics of different Au NPs are collected in Table 3.

4.3. Optical Limiting

OL materials based on noble metal nanoparticles are attractive, because gold and silver nanoparticles are easy to prepare, and they are highly soluble and stable in aqueous and organic solvents. The optical, nonlinear optical and optical limiting properties of gold and silver nanoparticles strongly depend on their size, shape, surrounding matrix, and solvent in which the nanoparticles are dissolved. Previously, considerable efforts have been focused on investigating the relationships between the OL and nonlinear optical properties of Au NPs and their size and shape (nanostars, nanospheres, nanorods, nanoshells, bipyramidal, etc). In the case of nanosecond pulses, the Au NPs exhibited intensity-dependent transformation from SA to RSA. Thus, Au NPs were found to display strong OL properties in the case of relatively long and

Table 3. Calculated nonlinear optical characteristics of four Au NPs. Reproduced from [59] with permission from Optical Society of America

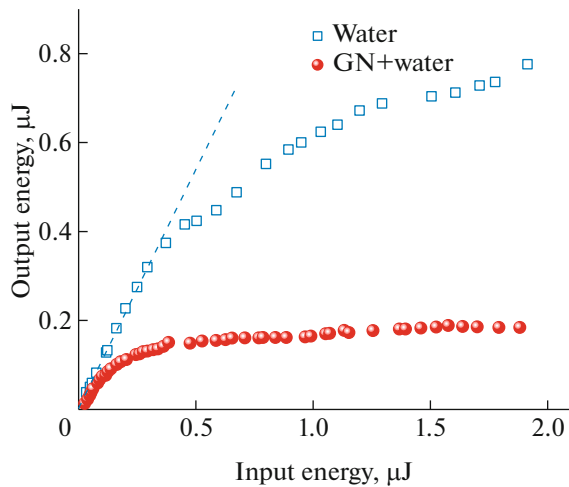|	Nonlinear optical characteristics of Au NPs			
	$\lambda = 800$ nm, $t = 60$ fs, 1 kHz, $E = 160$ nJ		$\lambda = 400$ nm, $t = 60$ fs, 1 kHz, $E = 38$ nJ	
Diameter	γ, cm^2/W ($\times 10^{-10}$)	β, cm/W ($\times 10^{-7}$)	γ, cm^2/W ($\times 10^{-10}$)	β, cm/W ($\times 10^{-7}$)
		OA		OA
64 nm	0.18	−0.7 ($I_{sat} = 5.7 \times 10^{-12}$ W/cm^2)	−2.3	−2.7 ($I_{sat} = 4 \times 10^{-11}$ W/cm^2)
32 nm	0.13	0.84	1	9
17 nm	0.14	0.59	2	7.2
13 nm	0.13	0.56	1.1	5.8

Fig. 12. Optical limiting of 800, 60 fs pulses in water and suspension containing 17 nm Au NPs. Reproduced from [59] with permission from Optical Society of America.
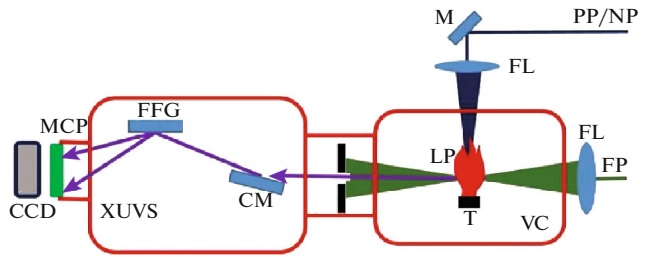

Fig. 13. High-order harmonic generation setup. FP, converting femtosecond pulses, PP/NP, picosecond or nanosecond heating pulses; FL, focusing lenses; VC, vacuum chamber; T, target; LP, laser plasma; XUVS, extreme ultraviolet spectrometer; CM, cylindrical gold-coated mirror; FFG, flat field grating; MCP, microchannel plate; CCD, CCD camera. Reproduced from [65] with permission from Hindawi.

high energy laser pulses [64]. The improved OL response in Au NPs has earlier been discussed from the viewpoint of structural characteristics.

In discussed studies, the OL was demonstrated using the 800 nm, 60 fs pulses propagating through the suspension containing 17 nm Au NPs in water. This effect is attributed to RSA. The suspension was placed close to the focal plane of 400 mm focal length lens. The energy of 800 nm pulses was gradually increased and then the output radiation propagated through the 2-mm-thick cell containing Au NPs suspension was measured. The linear dependence between input and output pulses was maintained up to the input pulse energy of ~0.11 μJ (Fig. 12, filled spheres). Further grow of input pulse energy led to OL of the energy of propagated laser radiation.

The energy of propagated pulse was stabilized at ~0.15–0.17 μJ. This process was maintained up to the input energy of 2 μJ above which stronger impeding processes worsened the propagation of laser pulses. Similar study in pure water showed no declination from the linear dependence up to $E_{\text{output}} \approx 0.35$ μJ of output radiation (Fig. 12, empty circles). At these conditions the coefficient of optical limiting induced suppression of propagating radiation in Au NPs suspension compared to pure water was measured to be ~2.5. Further growth of input energy (i.e., above $E_{\text{input}} = 0.4$ μJ) led to the growing influence of white light generation in water and declination of $E_{\text{input}}/E_{\text{output}}$ ratio from the linear dependence. Nevertheless, at highest used input energy ($E_{\text{input}} \approx 1.9$ μJ) the ~4-fold suppression of output pulses in Au NPs suspension compared to the pure water was achieved.

5. NONLINEAR OPTICAL STUDIES OF GOLD NANOPARTICLE FILMS

In this section, we analyze the third-order nonlinear optical properties and transient absorption of gold NP thin film as well as demonstrate the high-order harmonic generation from the ablated gold NP thin film [65].

The synthesis of Au NPs in solution was carried out by irradiation of the bulk gold target immersed in deionized water using 800 nm, 200 ps, 1 kHz pulses. The laser beam was focused by a 100 mm focal length lens on the bulk gold. Typically, the energy density of laser radiation on the metal surface was in the order of 10 J/cm². The irradiation of metal surface resulted in the fast removal of the material confined to the laser spot. The sample was displaced with regard to the laser beam, using a translating stage to avoid the formation of deep holes. The ablation was done for 10 minutes at continuous stirring. The Au film was prepared by evaporation of the aqueous suspension containing gold nanoparticles and then used as the target to perform the experiments. The thickness of thin film was examined by scanning electron microscope (SEM) to be approximately 100 nm. A noncollinear degenerate pump–probe technique and a Z-scan technique were employed to measure the transient absorption and nonlinear optical characteristics of Au NP films.

HHG in the plasmas produced during the ablation of Au NP thin film was performed using the setup shown in Fig. 13. The driving femtosecond pulses (800 nm, 30 fs, 1 kHz) propagated through the plasma formed by the nanosecond heating pulses (1064 nm, 5 ns, 10 Hz) at different delays between the heating and driving pulses. The harmonic yield was maximized by adjusting the position of the target. The generated high-order harmonics were analyzed by an extreme ultraviolet (XUV) spectrometer and detected by a microchannel plate with phosphor screen. The
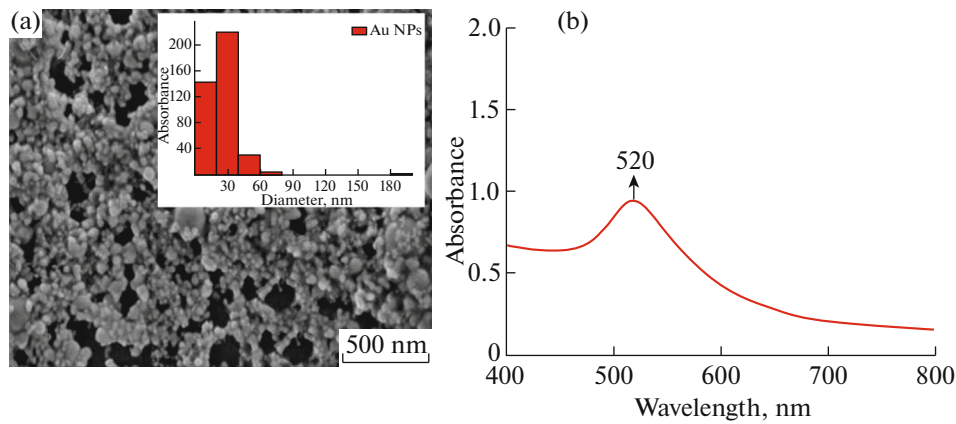
Fig. 14. (a) SEM image and size distribution of Au NPs. (b) Absorption spectrum of Au NP thin film. Reproduced from [65] with permission from Hindawi.

harmonic spectrum from the phosphor screen was imaged by a charge-coupled device (CCD) camera.

5.1. Low-order Nonlinearities of Au NP Film

SEM images and histograms of the Au NPs prepared by ablation of bulk gold using picosecond pulses are presented in Fig. 14a. The inset in Fig. 14a shows the size distribution of Au NPs, which covers the 10–90 nm range with mean size 30 nm. The sample shown in Fig. 14a was prepared by drying the drop of Au NP solution on the Si wafer or glass. Then this sample was analyzed by SEM. A few existing empty places in the SEM image had the sizes (<200 nm) significantly smaller than the area used for absorption measurements (5 × 5 mm) of the thin (~100 nm) gold film deposited on the silica glass plate. The presence of those tiny holes causes the insignificant variation of a whole spectral pattern. The absorption spectrum remained the same in different parts of deposited film due to the averaging of absorbance measured along the large area.

The absorption spectrum of thin film was analyzed in the range of 400 to 800 nm. The absorbance measurements were made using a 100 nm thin film. Figure 14b shows the absorption spectrum of Au NP thin film. The observed surface plasmon resonance of Au NPs was at 520 nm.

In the case of CA Z-scan measurements, the self-focusing was observed. The nonlinear refractive index was calculated from the fitting of the experimental CA curve. The nonlinear refractive index was calculated to be 2.6×10^{-11} cm^2 W^{-1}.

Figure 15 shows the OA and CA Z-scan curves of thin film. In the case of OA, the Au NP thin film showed SA, while close to focal area it demonstrated the RSA. The measured saturated intensity was 1.3×10^{10} W cm^{-2}. β_{RSA} was calculated from the fitting curve to be 9×10^{-6} cm W^{-1}. This value is one of largest

reported in the case of thin films measurements using different materials.

Time evolution of the absorption of probe pulses in the presence of pump pulses in the Au NP film at 400 nm is shown in Fig. 16. Prior to the TA measurements of the Au NP film deposited on a glass slide, the TA measurements of the pure glass slide were performed to separate its contribution from the former TA data. The pump–probe profile for thin gold film indicated the process of photobleaching due to excitation of the NPs under irradiation of 52 nJ, 400 nm, 35 fs pump pulses. In general, mechanisms of photoexcitation by femtosecond pulses in a metal include the excitation of electrons to a higher energy state through optical absorption, which leads the nonequilibrium electronic subsystem to relax via redistribution of the
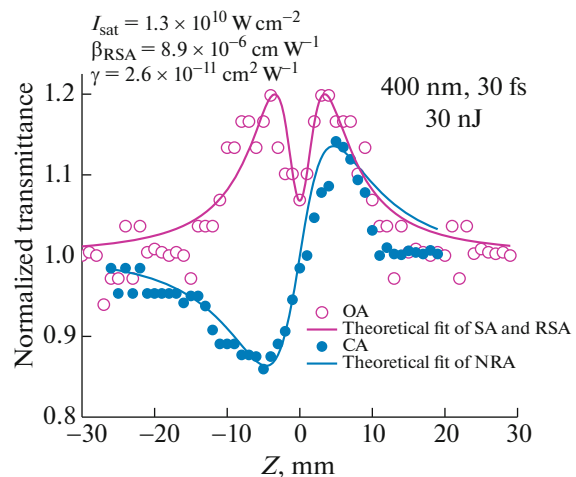

Fig. 15. OA and CA Z-scan curves of thin film measured using the 400 nm, 30 fs pulses. SA is saturable absorption; RSA is reverse saturable absorption; NRA is nonlinear refraction and absorption. Reproduced from [65] with permission from Hindawi.
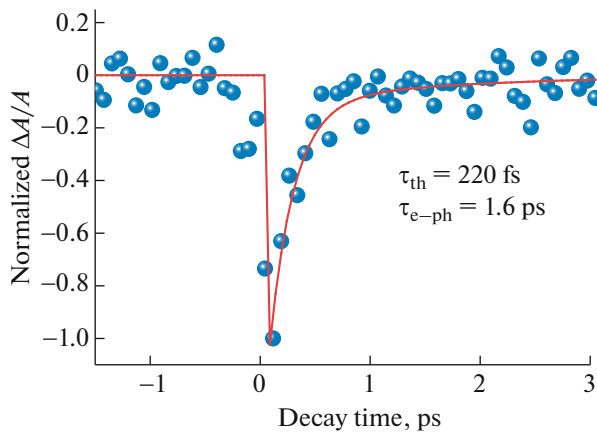
Fig. 16. Pump−probe dynamics of Au NP thin film at 400 nm. Reproduced from [65] with permission from Hindawi.

energy of excited electrons, typically known as electron−electron scattering interaction. The energy redistribution of the excited electrons occurs through electron−electron scattering within about 100−300 fs, which have been attributed to the electron thermalization process.

Another process of relaxation for excited electrons occurs via energy transfer of the electron to the lattice in the picosecond time scale due to electron−phonon interaction. In the present study, the employed pulse width (35 fs) of the femtosecond pulses was smaller than the decay time scale of the electron−electron relaxation dynamics in Au NPs. This made it feasible to probe the electron−electron dynamics. The fitting of the TA profile (Fig. 16, solid line) allowed determination of the time constants (τ_{th} = 220 fs and τ_{e-ph} = 1.6 ps) at λ = 400 nm. Here, τ_{th} and τ_{e-ph} are electron thermalization time constant and electron−phonon relaxation time constant.

5.2. High-order Harmonic Generation in Au NP Plasmas

The nanostructured materials can significantly enhance the harmonic yield in XUV range, since they have already demonstrated the ability to increase the second- and third-order nonlinear optical processes. Below we analyze the studies of high-order nonlinear optical processes in the plasma produced on the Au NP thin film deposited on glass substrates. HHG from the plasmas created on the bulk gold target and Au thin film were compared. The harmonics generated from the plasmas produced on the glass substrates, without thin film, were negligible compared with those from the plasmas produced on the bulk and metal thin films. In two cases, the plasma plumes were ablated using the 1064 nm, 5 ns heating pulses. The moderate intensity of heating pulses allowed the evaporation of

the neutral atoms and singly-charged ions from the targets during laser ablation. The advantages of the applications of neutral atoms and singly-charged ions for HHG have been demonstrated in a series of previous HHG studies in the laser-produced plasmas [66−68]. The optimal plasma plume was created by moving the target with regard to femtosecond beam propagation.

Figure 17a shows the harmonic spectra from the plasmas produced on the bulk Au and Au NP-contained thin films at 200 ns delay time between the heating and driving pulses. It was demonstrated that the harmonic intensity was significantly (approximately five times) enhanced in the case of Au NP thin film with regard to bulk Au. The experiments were carried out at different delays between the heating nanosecond and driving femtosecond pulses. Figure 17b shows the intensity variation of the eleventh harmonic with respect to different delay times. The maximum intensity of harmonics was achieved in the range of 200−500 ns delay times. During the ablation of thin film at optimal delays, the generation of the strong harmonics up to the 29th order was achieved. However, after crossing the delay of 800 ns the yield of harmonics was notably decreased.

The HHG from gas clusters has been reported in a few earlier studies [69−73]. Moreover, the harmonic generation in the plasmas containing plasmonic particles of different materials has also been analyzed to demonstrate the advantages of the proposed approach of HHG amendment [74−76]. In the plasma HHG studies, the nanoparticles were synthesized during laser ablation in a vacuum prior to formation of the NP-containing plasma plume or their appearance in the plasma was accomplished by ablation of commercially available nanoparticles.

The present research has demonstrated the preparation of gold nanoparticles during ablation of solid material in the liquid environment, deposition of synthesized NPs on the glass and silicon wafer, and ablation of thin deposited film in a vacuum to produce the plasma containing nanoparticles of narrow size distribution for harmonic generation at different delays between heating and driving pulses. Among them the most important novelty is the analysis of the role of the delay between the heating picosecond pulses creating nanoplasma and the driving femtosecond pulses generating harmonics on the HHG conversion efficiency. All previous HHG studies with nanoparticle-containing plasmas and gases were carried out at either fixed delay between heating and driving pulses (in the former case) or fixed distance from the nozzle of the gas jet [77, 78]. In previous plasma HHG studies, short delays of up to 100 ns between the heating and driving pulses were employed. It was not clear how heavy nanoparticle species could influence the processes of frequency conversion, because there was no proof of their presence in the interaction region with the driv-
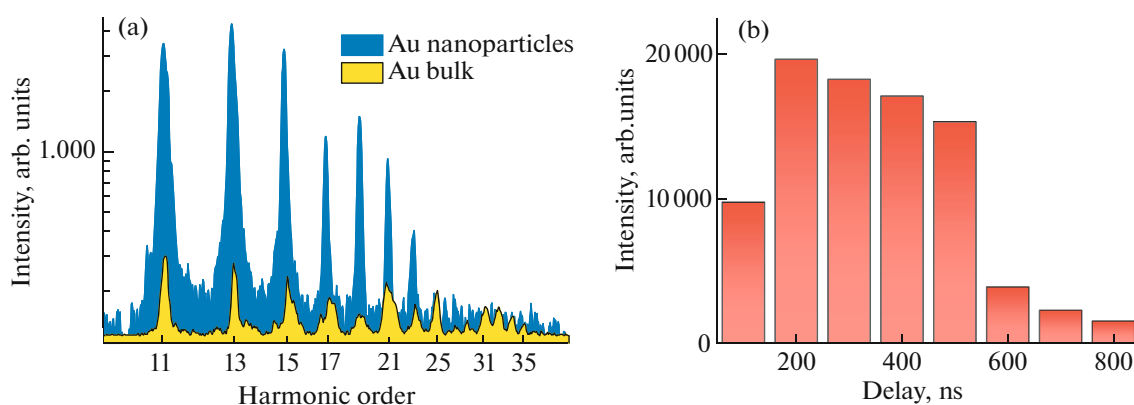
Fig. 17. (a) High-order harmonic spectra generated in the plasmas produced on the Au thin film and bulk Au. (b) Dependence of 11th harmonic yield on the delay between heating and driving pulses. Reproduced from [65] with permission from Hindawi.

ing laser (i.e., at the distance of a few hundred micrometers from the target surface), since one can expect their arrival in the region of the femtosecond laser beam propagation a few tens of microsecond from the beginning of ablation. One explanation was based on the disintegration of larger species into small clusters and monoatomic species, which probably could reach the interaction area at the short delays employed. However, no sufficient confirmation of this assumption has been provided.

To match the propagation of the driving pulse and the highest concentration of the studied group of multi-atomic species with a much larger delay, which cannot be achieved by optical methods, one therefore has to use the electronic methods of the adjustment of the delay between the heating and the driving pulses. The application of two electronically separated pulses from different lasers synchronized by a digital delay generator allows analysis of the involvement of various multi-particle species in the HHG process. Application of this approach for HHG in multi-particle plasmas, alongside with other methods of harmonic enhancement, requires the analysis of the dynamics of ablated species spreading out from the target to temporally match them with the propagation of driving femtosecond pulses through the plasma. One can expect the arrival of 30 nm particles in the region of the femtosecond laser beam propagation a few tens of microseconds from the beginning of ablation. Meanwhile, the discussed studies demonstrated the optimization of delays leading to the growth of harmonic yield in the case of Au NP plasma at around 200 ns. Below, we address this difference in the expected and actual optimal delay between heating and driving pulses in the case of Au NP-contained plasma.

In the case of a thermalized ablation plume, the average arrival times can be assigned to different cluster sizes. The delay between heating and driving pulses at which the harmonic yield reaches its maximum should scale as a square root of the atomic or molecu-

lar weight of the constituents. The ejection of lighter clusters from NPs allows them to reach the region of the driving beam earlier than heavier species. Therefore, NPs comprised of n atoms should appear in the interaction zone $n^{0.5}$ times later compared to single atoms, molecules, or ions of the sulfides. The additional studies revealed that, for bulk gold ablation, the maximum harmonic yield from single gold atoms and ions occurred at a delay of about 180−300 ns. Meantime, the Au NPs allowed efficient generation at about 200−400 ns delay (Fig. 17b), which is approximately equal to the delay in the case of Au atoms and ions. Furthermore, attempts to observe HHG at the delays of up to 50 μs (i.e., at the expected delay for thermalized larger nanoparticles) did not show any harmonic emission. Thus, the discussed studies demonstrated that NPs arrive at the area of interaction with the femtosecond laser beam notably earlier than one would expect for a thermalized ablation plume. In other words, all gold NPs acquire, from the very beginning, a similar kinetic energy and spread out from the surface with velocities approximately similar to those of the single gold atoms and ions ablating from bulk material. This conclusion reconciles the similarity in the optimal delays for HHG from bulk and NPs targets of the same material (Au).

It was suggested in [79] during their studies of third harmonic generation in plasma plumes that, at laser ablation characterized by the blast mechanism of laser−matter interaction, a similar average kinetic energy $E = mv^2/2$ could characterize all plasma components of the same elemental composition. Thus, the average arrival time assigned to the particles containing different amounts of identical atoms will be approximately the same, contrary to the case of slowly produced thermalized plasma. The studies of the high-order nonlinear optical processes occurring in the plasmas confirm this assumption. The difference in "optimal" delays between heating and driving

pulses is related to the difference in the velocities of particles, which depends on the atomic masses of the components of NPs. Similar conclusions have been reached during recent studies of HHG from the metal sulfide quantum dots [80].

6. SUMMARY

In this review, we have discussed different nonlinear optical properties of silver and gold nanoparticles. We have systematically analyzed the optical, structural, and nonlinear optical properties of 13 nm silver nanoparticles using probe pulses of different duration. The nonlinear optical properties of Ag NPs aqueous solutions prepared by chemical reduction method under different conditions were compared using the single beam Z-scan technique. The experimental results show that nonlinear absorption coefficient and nonlinear refractive index are strongly depend on the NPs concentration in solutions and the duration of probe pulses. In the case of picosecond probe pulses, the nonlinear absorption coefficient of Ag NPs at off-resonant conditions ($\lambda = 800$ nm) was four orders of magnitude lager than that in the case of femtosecond probe pulses. In the resonance case ($\lambda = 400$ nm), this ratio was also equal to four orders of magnitude.

For the nonlinear refractive indices, this value was approximately three orders of magnitude higher once compare the studies using picosecond and femtosecond probe pulses. OA Z-scans were also carried out close to resonance band of Ag NPs at the high concentration of Ag NPs aqueous solution under the conditions of application of the nanosecond pulses ($\lambda = 355$ nm). At different incident energies, the OA Z-scans showed the SA overpassed by RSA with the growth of laser pulse energy. The high and low pulse repetition rates were used for Z-scans to show that the repetition rate has no significant effect on the nonlinear optical characteristics of studied samples at used experimental conditions. In addition, the recovery time of these nonlinear processes was measured by a degenerate pump–probe transient absorption technique using 400 nm radiation ($\tau_1 = 3.9$ ps). The effect of beaching was observed with the increase of pump pulse fluence above 46 μJ/cm^2, which occurs beyond 10 ps time scale. Finally, we have demonstrated the optical limiting of Ag NPs using 800 nm, 60 fs pulses, which showed the two-fold decrease of propagated pulses at $E = 2.25$ μJ of incident radiation and stabilization of the optical limiting at the $E = 0.5$–0.6 μJ of output pulses.

We have further analyzed the Ag NPs prepared during ablation of bulk silver in deionized water using different wavelengths and durations of heating pulses. Their structural, optical and low-order nonlinear optical parameters were determined. The joint appearance of nonlinear optical refraction and absorption was analyzed using the 1064 nm, 5 ns and 800 nm, 60 fs probe pulses. The study of the nonlinear optical parameters of Ag NPs in the resonant and quasi-resonant conditions using 400 nm, 60 fs pulses have shown the presence of SA and RSA. The nonlinear absorption coefficient of suspensions was as high as 3.0×10^{-5} cm W^{-1} at the wavelength of 1064 nm. The Ag NP suspension has demonstrated the outstanding optical limiting properties in the case of 355 nm, 5 ns probe pulses. Nonlinear refraction showed the change of sign with variation of the wavelength and duration of laser pulses.

The lifetime of excited plasmon for Ag NPs at 400 nm was measured to be 2.5 ps, which can be assigned to the electron–phonon relaxation time. The excited state absorption cross sections of Ag NPs at different wavelengths were determined. The application of small-sized nanoparticles for low-order harmonic generation of femtosecond laser pulses was demonstrated and systematically analyzed during ablation of silver in air. The enhancement of low-order harmonic generation is attributed to the influence of silver clusters on the nonlinear optical response of Ag plasma. These studies, for the first time, have demonstrated the involvement of multi-atomic Ag particles in the growth of third harmonic yield. The conversion towards 266 nm radiation in the case of plasma plume was notably stronger compared with THG in air.

The selection of the topics of these studies followed with some logical sequences. OL effect is a process caused by the nonlinear optical properties of materials. It can be explained by z-scan data. We also analyzed the cross section of excited states using the saturable absorption data and transient absorption profile. Finally, it was demonstrated in the refereed studies, through harmonic generation, that ablation and formation of nanoparticles in liquid and air has the advantages, which can be used for high-order harmonic generation in the laser-produced silver plasmas containing nanoparticles and quantum dots. Furthermore, the increase of third harmonic yield in the plasmas containing silver nanoparticles allows basic explanation of the formation silver nanoparticles at different conditions.

The Au NPs has been of the significant importance due to their use for surface-enhanced Raman scattering. We analyzed four groups (with the sizes of 13, 17, 32, and 64 nm) of Au NPs of different sizes at 400 and 800 nm using the 60 fs pulses propagating through the Au NPs suspensions. The plasmonic resonance of Au NPs is far from 800 nm. We analyzed the optical, structural, and nonlinear optical characteristics of Au NPs suspensions synthesized by chemical method. Their nonlinear refractive indices, nonlinear absorption coefficients, and saturated intensities were measured. We also discussed the optical limiting of 800 nm, 60 fs pulses in 17 nm Au NPs suspension and showed approximately four-fold limitation of propagated pulses with regard to the pure water. The compe-

tition of saturable and reverse saturable absorption in the case of 800 nm pulses were analyzed at different energies of laser pulses.

As it was shown in discussed studies, the nanorods, nanocubes, and nanoparticles of the same metal show completely different properties. That is the reason why many groups are working to develop different methods of synthesis of the metallic nanoparticles and particularly Au NPs. The discussed work was aimed in the search of size-dependent nonlinear optical properties of GN at 400 nm (i.e., near the plasmonic resonance) and 800 nm (i.e., out of the plasmonic resonance). The calculation of the β in the case of RSA (7×10^{-6} cm W^{-1}) in Au NPs is among the largest reported so far for the metal nanoparticles. The intensity-dependent transformation from saturable absorption to reverse saturable absorption and excellent optical response indicate that the small-sized Au NPs can be considered as potential candidate in passive mode locking and eye/device protection against powerful lasers.

Finally, we have discussed the studies of the gold nanoparticle-contained thin film prepared by evaporation of the Au NP suspension, which was synthesized by laser ablation. The Au NP thin film was characterized using the UV-visible absorption spectra and SEM analysis. We have analyzed the origin of strong nonlinear absorption (9×10^{-6} cm W^{-1}) in this film at 400 nm. The thin film exhibited a switch from SA to RSA at stronger excitation. The relaxation time of SA was measured to be 1.6 ps. The high-order harmonic generation was analyzed in the plasma containing gold nanoparticles. The HHG efficiency in that case was ten times higher compared with the case of bulk gold ablation. For the first time, the effective application of the ablated 100 nm thin film of gold nanoparticles for harmonic generation in the 27−115 nm range was achieved.

Overall, the Ag and Au NPs have demonstrated the advanced nonlinear optical properties, which can be further used in different areas of optoelectronics.

REFERENCES

1. C. C. Lu, X. Y. Hu, K. B. Shi, Q. Hu, R. Zhu, H. Yang, and Q. H. Gong, Light: Sci. Appl. **4**, 302 (2015).

2. Y. Feng, Q. Yao, J. Li, N. Goswami, J. Xie, and J. Yang, Nano Res. **9**, 942 (2016).

3. C. C. M. Neumann, E. Laborda, K. Tschulik, K. R. Ward, and R. G. Compton, Nano Res. **6**, 511 (2013).

4. A. Hernández-Arteaga, J. J. Z. Nava, E. S. Kolosovas-Machuca, J. J. Velázquez-Salazar, E. Vinogradova, M. José-Yacamán, and H. R. Navarro-Contreras, Nano Res. **10**, 3662 (2017).

5. K. Tschulik, B. Haddou, D. Omanović, N. V. Rees, and R. G. Compton, Nano Res. **6**, 836 (2013).

6. R. A. Ganeev, J. Opt. A **7**, 717 (2005).

7. R. A. Ganeev, A. I. Ryasnyansky, S. R. Kamalov, M. K. Kodirov, and T. Usmanov, J. Phys. D **34**, 1602 (2001).

8. G. K. Podagatlapalli, S. Hamad, S. P. Tewari, S. Sreedhar, M. D. Prasad, and S. V. Rao, J. Appl. Phys. **113**, 073106 (2013).

9. G. H. Fan, S. L. Qu, Z. Y. Guo, Q. Wang, and Z. L. Li, Chin. Phys. B **21**, 047804 (2012).

10. R. A. Ganeev, M. Baba, A. I. Ryasnyansky, M. Suzuki, and H. Kuroda, Opt. Spectrosc. **99**, 668 (2005).

11. J. Jayabalan, A. Singh, R. Chari, and S. M. Oak, Nanotechnol. **18**, 315704 (2007).

12. S. Porel, N. Venkatram, D. Narayana Rao, and T. P. Radhakrishnan, J. Appl. Phys. **102**, 033107 (2007).

13. O. Muller, S. Dengler, G. Ritt, and B. Eberle, Appl. Opt. **52**, 139 (2013).

14. R. A. Ganeev, M. Baba, A. I. Ryasnyansky, M. Suzuki, and H. Kuroda, Appl. Phys. B **80**, 595 (2005).

15. C. H. Bae, S. H. Nam, and S. M. Park, Appl. Sur. Sci. **197−198**, 628 (2002).

16. M. López-Arias, M. Oujja, M. Sanz, R. A. Ganeev, G. S. Boltaev, N. K. Satlikov, R. I. Tugushev, T. Usmanov, and M. Castillejo, J. Appl. Phys. **111**, 043111 (2012).

17. R. A. Ganeev, H. Singhal, P. A. Naik, J. A. Chakera, M. Tayyb, A. K. Srivastava, T. S. Dhami, M. P. Joshi, A. Singh, R. Chari, S. R. Kumbhare, R. P. Kushwaha, R. A. Khan, and P. D. Gupta, Opt. Spectrosc. **108**, 787 (2010).

18. A. L. Stepanov, C. Marques, E. Alves, R. C. da Silva, M. R. Silva, R. A. Ganeev, A. I. Ryasnyansky, and T. Usmanov, Tech. Phys. Lett. **31**, 702 (2005).

19. R. A. Ganeev and T. Usmanov, Quantum Electron. **37**, 605 (2007).

20. D. Wu, J. Peng, Z. Cai, J. Weng, Z. Luo, N. Chen, and H. Xu, Opt. Express **23**, 24071 (2015).

21. L. W. Tutt and A. Kost, Nature (London, U.K.) **356**, 225 (1992).

22. N. Venkatram, D. N. Rao, and M. A. Akundi, Opt. Express **13**, 867 (2005).

23. R. A. Ganeev, H. Singhal, P. A. Naik, J. A. Chakera, M. Tayyb, A. K. Srivastava, T. S. Dhami, M. P. Joshi, A. Singh, R. Chari, S. R. Kumbhare, R. P. Kushwaha, R. A. Khan, and P. D. Gupta, Opt. Spectrosc. **108**, 787 (2010).

24. E. Fazio, D. Hulin, V. Chumash, F. Michelotti, A. M. Andriesh, and M. Bertolotti, J. Non. Cryst. Solids **168**, 213 (1994).

25. K. Anshu and A. Sharma, Optik **127**, 48 (2016).

26. A. L. Dawar, P. K. Shishodia, G. Chauhan, J. C. Joshi, C. Jagadish, and P. C. Mathur, Appl. Opt. **29**, 1971 (1990).

27. J. Olesiak-Banska, M. Gordel, R. Kolkowski, K. Matczyszyn, and M. Samoc, J. Phys. Chem. C **116**, 13731 (2012).

28. J. Lv, L. Jiang, C. Li, X. Liu, M. Yuan, J. Xu, W. Zhou, Y. Song, H. Liu, and Y. Li, Langmuir **24**, 8297 (2008).

29. M. Tajdidzadeh, A. B. Zakaria, Z. AbidinTalib, A. S. Gene, and S. Shirzadi, J. Nanomater. **480**, 3843 (2017).

30. D. D. Smith, Y. Yoon, R. W. Boyd, J. K. Campbell, L. A. Baker, and R. M. Crooks, J. Appl. Phys. **86**, 11 (1999).

31. R. West, Y. Wang, and T. Goodson III, J. Phys. Chem. B **107**, 15 (2003).

32. K. Wang, H. Long, M. Fu, G. Yang, and P. Lu, Opt. Lett. **35**, 1560 (2010).

33. A. I. Ryasnyanskiy, B. Palpant, S. Debrus, U. Pal, and A. Stepanov, J. Lumin. **127**, 181 (2007).

34. R. A. Ganeev, M. Suzuki, M. Baba, M. Ichihara, and H. Kuroda, J. Appl. Phys. **103**, 063102 (2008).

35. C. Zheng, W. Li, W. Chen, and X. Ye, Mater. Lett. **116**, 1 (2014).

36. K. Zhang, R. A. Ganeev, K. S. Rao, S. K. Maurya, G. S. Boltaev, P. S. Krishnendu, Z. Yu, W. Yu, Y. Fu, and C. Guo, J. Nanomater. **60**, 56528 (2019).

37. J.-Y. Bigot, V. Halte, J.-C. Merle, and A. Daunois, Chem. Phys. **251**, 181 (2000).

38. G. S. Boltaev, R. A. Ganeev, P. S. Krishnendu, S. K. Maurya, P. V. Redkin, K. S. Rao, K. Zhang, and C. Guo, Appl. Phys. A **124**, 766 (2018).

39. R. A. Ganeev, J. Opt. A **7**, 717 (2005).

40. Y.-P. Sun, J. E. Riggs, H. W. Rollins, and R. Guduru, J. Phys. Chem. B **103**, 77 (1999).

41. R. A. Ganeev, A. S. Zakirov, G. S. Boltaev, R. I. Tugushev, T. Usmanov, P. K. Khabibullaev, T. W. Kang, and A. A. Saidov, Opt. Mater. **33**, 419 (2011).

42. R. Sato, M. Ohnuma, K. Oyoshi, and Y. Takeda, J. Appl. Phys. **117**, 113101 (2015).

43. K. Kim and S. Choe, Plasmonics **12**, 855 (2017).

44. V. Halte, J.-Y. Bigot, B. Palpant, M. Broyer, B. Prével, and A. Pérez, Appl. Phys. Lett. **75**, 3799 (1999).

45. H. Sanchez-Esquivel, K. Y. Raygoza-Sanchez, R. Rangel-Rojo, B. Kalinic, N. Michieli, T. Cesca, and G. Mattei, Nanoscale **10**, 5182 (2018).

46. A. I. Ryasnyansky, R. A. Ganeev, and M. K. Kodirov, Opt. Spectrosc. **94**, 627 (2003).

47. R. A. Ganeev, P. A. Naik, H. Singhal, U. Chakravarty, V. Arora, J. A. Chakera, R. A. Khan, M. Raghuramaiah, S. R. Kumbhare, R. P. Kushwaha, and P. D. Gupta, Opt. Spectrosc. **103**, 831 (2007).

48. R. A. Ganeev, Opt. Spectrosc. **125**, 982 (2018).

49. R. A. Ganeev, H. Singhal, P. A. Naik, J. A. Chakera, M. Kumar, and P. D. Gupta, Phys. Rev. A **82**, 043812 (2010).

50. G. Ramakrishna, O. Varnavski, J. Kim, D. Lee, and T. Goodson, J. Am. Chem. Soc. **130**, 5032 (2008).

51. Y. Yang, M. Nogami, J. Shi, H. Chen, G. Ma, and S. Tang, Appl. Phys. Lett. **8**, 081110 (2006).

52. I. Mirza, D. McCloskey, W. J. Blau, and J. G. Lunney, Opt. Lett. **43**, 1455 (2018).

53. L. D. Boni, E. L. Wood, C. Toro, and F. E. Hernandez, Plasmonics **3**, 171 (2008).

54. H. I. Elim, J. Yang, J. Y. Lee, J. Mi, and W. Ji, Appl. Phys. Lett. **88**, 083107 (2006).

55. K. S. Lee and M. A. El-Sayed, J. Phys. Chem. B **109**, 20331 (2005).

56. X. Liu, X. Jia, M. Fischer, Z. Huang, and D. R. Smith, Nano Lett. **18**, 6181 (2018).

57. R. A. Ganeev, A. I. Ryasnyanskiy, A. L. Stepanov, T. Usmanov, C. Marques, R. C. da Silva, and E. Alves, Opt. Spectrosc. **101**, 615 (2006).

58. J. T. Seo, Q. Yang, W. J. Kim, J. Heo, S. Ma, J. Austin, W. S. Yun, S. S. Jung, S. W. Han, B. Tabibi, and D. Temple, Opt. Lett. **34**, 307 (2009).

59. Y. Fu, R. A. Ganeev, P. S. Krishnendu, C. Zhou, K. S. Rao, and C. Guo, Opt. Mater. Express **9**, 976 (2019).

60. X. Ji, X. Song, J. Li, Y. Bai, W. Yang, and X. Peng, J. Am. Chem. Soc. **129**, 13939 (2007)

61. P. N. Njoki, I. I. S. Lim, D. Mott, H.-Y. Park, B. Khan, S. Mishra, R. Sujakumar, J. Luo, and C.-J. Zhong, J. Phys. Chem. C **111**, 14664 (2007).

62. M. A. Villegas, M. A. Garcia, J. Llopis, and J. M. Fernandez Navarro, J. Sol−Gel Sci. Technol. **11**, 251 (1998).

63. K. Wang, H. Long, M. Fu, G. Yang, and P.-X. Lu, Chin. Phys. Lett. **27**, 124204 (2010).

64. C. Zheng, J. Huang, L. Lei, W. Chen, H. Wang, and W. Li, Appl. Phys. B **124**, 17 (2018).

65. A. Rout, G. S. Boltaev, R. A. Ganeev, Y. Fu, S. K. Maurya, V. V. Kim, K. S. Rao, and C. Guo, Nanomater. **9**, 291 (2019).

66. R. A. Ganeev and H. Kuroda, Opt. Spectrosc. **100**, 937 (2006).

67. R. A. Ganeev, L. B. ElougaBom, and T. Ozaki, Opt. Spectrosc. **108**, 970 (2010).

68. R. A. Ganeev, Opt. Spectrosc. **122**, 250 (2017).

69. T. D. Donnelly, T. Ditmire, K. Neuman, M. D. Perry, and R. W. Falcone, Phys. Rev. Lett. **76**, 2472 (1996).

70. J. W. G. Tisch, T. Ditmire, D. J. Fraser, N. Hay, M. B. Mason, E. Springate, J. P. Marangos, and M. H. R. Hutchinson, J. Phys. B **30**, L709 (1997).

71. C. Vozzi, M. Nisoli, J.-P. Caumes, G. Sansone, S. Stagira, S. de Silvestri, M. Vecchiocattivi, D. Bassi, M. Pascolini, L. Poletto, P. Villoresi, and G. Tondello, Appl. Phys. Lett. **86**, 111121 (2005).

72. S. X. Hu and Z. Z. Xu, Appl. Phys. Lett. **71**, 2605 (1997).

73. H. Ruf, C. Handschin, R. Cireasa, N. Thiré, A. Ferré, S. Petit, D. Descamps, E. Mével, E. Constant, V. Blanchet, B. Fabre, and Y. Mairesse, Phys. Rev. Lett. **110**, 083902 (2013).

74. R. A. Ganeev, M. Suzuki, M. Baba, M. Ichihara, and H. Kuroda, J. Phys. B **41**, 045603 (2008).

75. R. A. Ganeev, Opt. Spectrosc. **105**, 777 (2008).

76. R. A. Ganeev, P. A. Naik, H. Singhal, U. Chakravarty, V. Arora, J. A. Chakera, R. A. Khan, M. Raghuramaiah, S. R. Kumbhare, R. P. Kushwaha, and P. D. Gupta, Opt. Spectrosc. **103**, 795 (2007).

77. R. A. Ganeev, Opt. Spectrosc. **124**, 521 (2018).

78. R. A. Ganeev, Opt. Spectrosc. **124**, 855 (2018)

79. R. De Nalda, M. López-Arias, M. Sanz, M. Oujja, and M. Castillejo, Phys. Chem. Chem. Phys. **13**, 10755 (2011).

80. R. A. Ganeev, G. S. Boltaev, V. V. Kim, K. Zhang, A. I. Zvyagin, M. S. Smirnov, O. V. Ovchinnikov, P. V. Redkin, M. Wöstmann, H. Zacharias, and C. Guo, Opt. Express **26**, 35013 (2018).